

# JGR Solid Earth

## RESEARCH ARTICLE

10.1029/2022JB024693

### Key Points:

- Five minutes sampled Global Positioning System supplemented with InSAR resolves a shallow slow slip event, which preceded the swarm by 2–15 hr
- Seismicity was driven in the early stage by the slow slip event with nonlinear expansion and later by fluid with propagating back front
- A stress-driven model explains the overall evolution of seismicity and provides constraints on friction and fluid pressure

### Supporting Information:

Supporting Information may be found in the online version of this article.

### Correspondence to:

K. Sirorattanakul,  
ksirorat@caltech.edu

### Citation:

Sirorattanakul, K., Ross, Z. E., Khoshmanesh, M., Cochran, E. S., Acosta, M., & Avouac, J.-P. (2022). The 2020 Westmorland, California earthquake swarm as aftershocks of a slow slip event sustained by fluid flow. *Journal of Geophysical Research: Solid Earth*, 127, e2022JB024693. <https://doi.org/10.1029/2022JB024693>

Received 2 MAY 2022

Accepted 7 NOV 2022

### Author Contributions:

**Conceptualization:** Krittanon Sirorattanakul, Zachary E. Ross, Jean-Philippe Avouac

**Data curation:** Krittanon Sirorattanakul, Zachary E. Ross, Mostafa Khoshmanesh, Elizabeth S. Cochran

**Formal analysis:** Krittanon Sirorattanakul, Zachary E. Ross, Mostafa Khoshmanesh, Elizabeth S. Cochran, Mateo Acosta, Jean-Philippe Avouac

**Funding acquisition:** Zachary E. Ross, Jean-Philippe Avouac

© 2022. The Authors.

This is an open access article under the terms of the [Creative Commons Attribution License](https://creativecommons.org/licenses/by/4.0/), which permits use, distribution and reproduction in any medium, provided the original work is properly cited.

# The 2020 Westmorland, California Earthquake Swarm as Aftershocks of a Slow Slip Event Sustained by Fluid Flow

Krittanon Sirorattanakul<sup>1</sup> , Zachary E. Ross<sup>1</sup> , Mostafa Khoshmanesh<sup>2</sup>, Elizabeth S. Cochran<sup>3</sup> , Mateo Acosta<sup>1</sup> , and Jean-Philippe Avouac<sup>1,2</sup> 

<sup>1</sup>Seismological Laboratory, Division of Geological and Planetary Sciences, California Institute of Technology, Pasadena, CA, USA, <sup>2</sup>Department of Mechanical and Civil Engineering, California Institute of Technology, Pasadena, CA, USA, <sup>3</sup>United States Geological Survey, Earthquake Science Center, Pasadena, CA, USA

**Abstract** Swarms are bursts of earthquakes without an obvious mainshock. Some have been observed to be associated with transient aseismic fault slip, while others are thought to be related to fluids. However, the association is rarely quantitative due to insufficient data quality. We use high-quality GPS/GNSS, InSAR, and relocated seismicity to study a swarm of >2,000 earthquakes which occurred between 30 September and 6 October 2020, near Westmorland, California. Using 5 min sampled Global Positioning System (GPS) supplemented with InSAR, we document a spontaneous shallow  $M_w$  5.2 slow slip event that preceded the swarm by 2–15 hr. The earthquakes in the early phase were predominantly non-interacting and driven primarily by the slow slip event resulting in a nonlinear expansion. A stress-driven model based on the rate-and-state friction successfully explains the overall spatial and temporal evolution of earthquakes, including the time lag between the onset of the slow slip event and the swarm. Later, a distinct back front and a square root of time expansion of clustered seismicity on en-echelon fault structures suggest that fluids helped sustain the swarm. Static stress triggering analysis using Coulomb stress and statistics of interevent times suggest that 45%–65% of seismicity was driven by the slow slip event, 10%–35% by inter-earthquake interactions, and 10%–30% by fluids. Our model also provides constraints on the friction parameter and the pore pressure and suggests that this swarm behaved like an aftershock sequence but with the mainshock replaced by the slow slip event.

**Plain Language Summary** Over 2,000 earthquakes were recorded near Westmorland, California, between 30 September and 6 October 2020. Such an increased level of earthquake activity is quite common in this region, though the causes are not well-understood. Using available seismological data, satellite imagery, and ground-based GPS/GNSS, we detect ground deformations a few hours before the increased earthquake activity. We map these ground deformations to motion along the faults at a depth shallower than 5 km. We show that this silent fault slip drove the earthquakes at a greater depth of 5–8 km. The overall spatial and temporal evolution of the earthquakes can be largely predicted based on the stress changes imparted by this silent fault slip. Statistical analysis of earthquake activity and the expansion of the zone with no earthquake further suggest that fluids played a significant role in sustaining the earthquake sequence. Though we can explain earthquake activity after the initial ground deformations, what causes the initial fault motion at depth and thus these ground deformations in the first place remains an open question.

## 1. Introduction

Earthquakes are often seen to cluster in time and space. Many clusters have a clearly identifiable mainshock followed by numerous smaller aftershocks. Others occur as a sustained burst of small magnitude earthquakes lasting from hours to several years without an obvious mainshock, referred to as a swarm (Mogi, 1963). The peak seismicity rate during swarms can reach >10,000 times the background level with complex temporal evolution that cannot be explained by the simple Omori-Utsu type power-law decay (Omori, 1894; Utsu, 1961) typical of mainshock-aftershock sequences (Holtkamp & Brudzinski, 2011; Vidale & Shearer, 2006). Swarms also often expand spatially (X. Chen et al., 2012) with a velocity ranging from m/day (e.g., Ross et al., 2020) to km/hr (e.g., Roland & McGuire, 2009). Swarms can occur in a wide range of geological settings, such as volcanoes (e.g., Shelly & Hardebeck, 2019; Wicks et al., 2011; Yukutake et al., 2011), subduction zones (e.g., Holtkamp & Brudzinski, 2011; Hoskins et al., 2021; Nishikawa & Ide, 2017), transform faults (e.g., Roland & McGuire, 2009), hydrothermal systems (e.g., Heinicke et al., 2009), stable continental regions (Sharma et al., 2020), and reservoirs with anthropogenic hydraulic stimulations (e.g., Im & Avouac, 2021; Wei et al., 2015). In some cases, swarms can

**Supervision:** Zachary E. Ross, Jean-Philippe Avouac  
**Writing – original draft:** Krittanon Siroattanakul, Jean-Philippe Avouac  
**Writing – review & editing:** Zachary E. Ross, Mostafa Khoshmanesh, Elizabeth S. Cochran, Mateo Acosta

include larger destructive earthquakes (Chiaraluce et al., 2011; Nishikawa & Ide, 2018). The epidemic-type aftershock sequence model (Ogata, 1988, 1992), based on empirical laws, can reproduce different regimes of seismicity evolution, including standard Omori-type aftershocks and swarm sequences (Helmstetter & Sornette, 2002b). However, in terms of their mechanics, why spatiotemporal evolutions of swarms are fundamentally different from mainshock-aftershock sequences remains poorly understood.

The seismicity evolution during a swarm is often thought to be governed by external aseismic processes such as a slow slip event, fluid flow, magma intrusion, or a combination. Transient aseismic fault slip in the form of a slow slip event can increase shear stress on neighboring fault patches and has in particular been associated with swarms along oceanic transform faults (e.g., Roland & McGuire, 2009) and extensional or transtensional continental fault systems (e.g., Gualandi et al., 2017; Jiang et al., 2022; Lohman & McGuire, 2007; Martínez-Garzón et al., 2021; Passarelli et al., 2015). Alternatively, elevated pore pressure from fluid flow or magmatic intrusion can decrease effective normal stress, thus reducing fault strength and bringing the faults closer to failure (e.g., Dieterich et al., 2000; Hubbert & Rubey, 1959; Nur & Booker, 1972). This mechanism has been associated with swarms in volcanic (e.g., Cappa et al., 2009; Fischer et al., 2014; Hainzl et al., 2016; Roman & Cashman, 2006; Shelly et al., 2016, 2013) and hydrothermal settings (e.g., Audin et al., 2002; Got et al., 2011). Fluid-driven swarms are expected to expand as a square root of time, as observed in seismicity induced by anthropogenic fluid injections (e.g., Shapiro et al., 1997, 2002). In many examples, such as in the Corinth rift (De Barros et al., 2020; Dublanchet & De Barros, 2021), in Nevada (Hatch et al., 2020), and in situ fault slip reactivation experiments (Guglielmi et al., 2015), pore-pressure changes can induce propagating slow slip fronts leading to a coupled process (e.g., Bhattacharya & Viesca, 2019; Dublanchet, 2019; Larochelle et al., 2021; Sáez et al., 2022; Yukutake et al., 2022). A few studies, such as those for the 2000 Izu volcanic swarm (Toda et al., 2002) and earthquakes on Kilauea volcano, Hawaii (Segall et al., 2006), have demonstrated that nucleation models based on rate-and-state friction (Dieterich, 1994; Heimissson & Segall, 2018) can explain how seismicity responds to these external forcings.

In this study, we focus on the Westmorland swarm, which occurred between 30 September and 6 October 2020, near Westmorland, California (Figure 1), in a setting (Section 2) where swarms are common and where some have been associated with slow slip events (X. Chen & Shearer, 2011; Lohman & McGuire, 2007; Materna et al., 2022; Wei et al., 2015). We utilize a newly available data set, including seismic data, daily and 5 min sampled Global Positioning System (GPS) position time series, and interferometric synthetic aperture radar (InSAR), to image the time evolution of ground deformations as the swarm unfolds (Section 3). This unique data set and the advanced data processing techniques allow us to extract the complete time evolution of ground deformation during the swarm and explore the spatio-temporal relationship between seismicity and the slow slip event in detail (Sections 4 and 5). Our observations and modeling results demonstrate that the 2020 Westmorland swarm was driven predominantly in the early stage by the slow slip event with limited inter-earthquake interactions and later by pore-pressure diffusion (Section 6).

## 2. Seismotectonic Setting

The 2020 Westmorland swarm sequence began around 22:00 UTC on 30 September 2020, and lasted for approximately 140 hr until 18:00 UTC on 6 October 2020. The sequence was located in the Brawley Seismic Zone of the Salton Trough (Figure 1) along the North American-Pacific plate boundary at the transition between the right-lateral strike-slip San Andreas Fault (SAF) and the ridge transform system in the Gulf of California (Brothers et al., 2009). The region hosts a mixture of left-lateral strike-slip step-over faults that connect shorter segments of the main right-lateral strike-slip fault (C. E. Johnson & Hill, 1982), primarily accommodating the extensional crustal stress field (Yang & Hauksson, 2013). The fault zone accounts for 17 mm/yr of right-lateral shear parallel to the SAF (Crowell et al., 2013), roughly one-third of the long-term plate rate (Argus et al., 2011; Bird, 2003). The Coachella segment of the SAF just north of the Salton Trough has a very low seismicity rate and is generally regarded to be mostly locked (e.g., Lindsey & Fialko, 2013), with the last major earthquake occurring about 320 yr ago (Rockwell et al., 2016). The frequent seismic swarms in the Salton Trough (Lohman & McGuire, 2007) pose concerns about the possibility of the swarms triggering a large earthquake on the SAF (Hauksson et al., 2017).

In this region, the sedimentary cover is 5 km thick (Fuis et al., 1984) and composed mostly of quartz and calcite (Younker et al., 1982). The basement comprises primarily metasedimentary units (Fuis et al., 1984) that

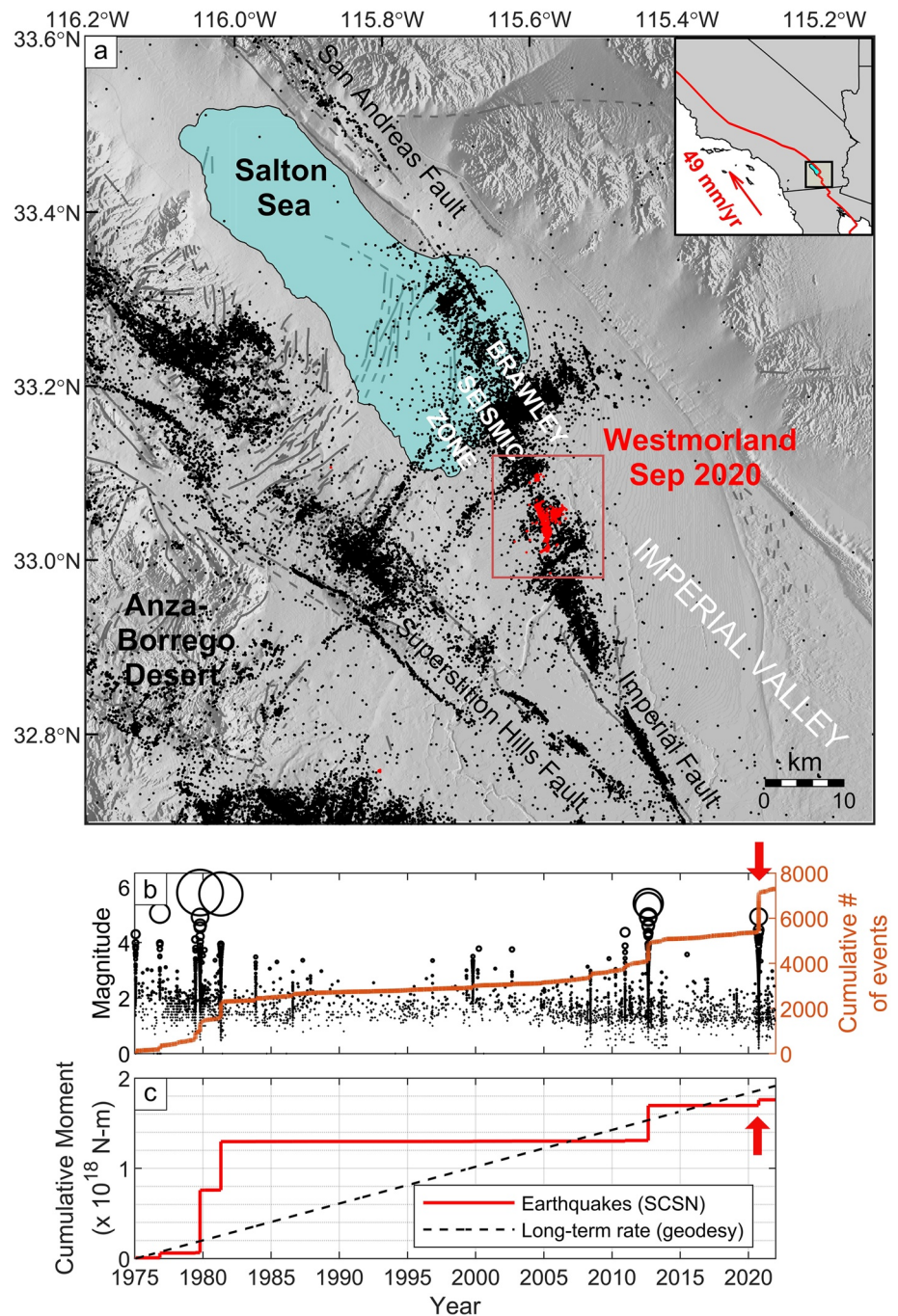


**Figure 1.** (a) Regional map of 1981–2019 relocated seismicity from the Hauksson-Yang-Shearer (HYS) catalog (Hauksson et al., 2012) shown as black dots. This study's high-resolution relocated seismicity catalog of the 2020 Westmorland swarm is shown as red dots. The mapped Quaternary faults are from the United States Geological Survey (USGS) QFaults database (USGS, 2019). The North American-Pacific plate boundary location (red line in inset) is from Bird (2003). Shorelines are from Wessel and Smith (1996). Salton Sea outline is from Google Earth images (Google Earth V 7.3, 2020). (b) Seismicity records from the Southern California Seismic Network (SCSN) catalog (Hutton et al., 2010) from 1975 to 2021 over the Westmorland area (red box in panel a) with a consistent completeness magnitude of 1.4 over the entire duration (Figure S1 in Supporting Information S1). (c) Comparison between the cumulative moment release of seismicity (SCSN catalog) and long-term geodetic strains near the Westmorland area (red box in panel a). Only geodetic strains across the seismogenic depths, constrained from our relocated seismicity catalog (Figure 2) to be between 4.5 and 8.5 km, are considered. Geodetic moment release is estimated using the mean slip rate of 17 mm/yr (Crowell et al., 2013) and a shear modulus of 30 GPa. During the 2020 Westmorland swarm (annotated by red arrows in panels (b) and (c)), there was a relatively large jump in the cumulative number of events but only a modest increase in seismic moment release.

have undergone significant metamorphism due to a high-temperature gradient of 50–60°C/km (Lachenbruch et al., 1985). Deeper than 10–16 km, the crust mainly consists of diabase and gabbro (Fuis et al., 1984). Since mud pots and hydro-volcanic events are common in the Salton Trough (Robinson & Elders, 1976), abundant fluids and high geothermal gradients could play a significant role in swarm initiation (Ben-Zion & Lyakhovskiy, 2006).

### 3. Data Processing

#### 3.1. Seismicity

We use a machine learning workflow for earthquake monitoring (Ross & Cochran, 2021) to build a high-resolution relocated seismicity catalog. We summarize the key steps and point to references in which the methods are described in detail.

First, we aim to detect earthquakes on individual three-component traces. We start from the raw continuous waveform data from 47 regional seismic stations (Figure S2 in Supporting Information S1) processed by the Southern California Earthquake Data Center (SCEDC, 2013) and apply a deep learning phase detector/picker model originally trained by Ross et al. (2020). This network takes in 16 s windows of three-component data and outputs the likelihood of *P* waves and *S* waves at each time step. We set a threshold of the peak sigmoid probability of 0.5 to trigger a detection and record the time at which the threshold is first exceeded. This is repeated for all stations and all days of data. Next, we associate the detected phases at individual stations to particular earthquakes using the PhaseLink deep learning-based association algorithm (Ross, Yue, Meier, Hauksson, & Heaton, 2019). Because the station distribution and local seismic velocity structure differ, we re-train the neural network following Ross, Trugman, Hauksson, & Shearer (2019) and Ross, Yue, et al. (2019) and use the exact settings for the associator described in Ross and Cochran (2021). Once the association process is completed, we locate the events using HypoSVI (Smith et al., 2021), a variational Bayesian method. We use the Southern California Earthquake Center Community Velocity Model CVM-H (Shaw et al., 2015) and keep all tunable parameters the same as in Smith et al. (2021).

Finally, we relocate the seismicity with waveform cross-correlation. We correlate all possible pairs of events using 1.0 s windows starting 0.1 s before each pick using 1–20 Hz filtered waveforms. We retain differential times with a peak correlation coefficient of at least 0.6 and have a correlation difference between the positive and negative maxima of at least 0.2. Then, we use these differential times as the input to GrowClust (Trugman & Shearer, 2017), a cluster-based double-difference relocation algorithm. Since GrowClust works only with 1D velocity models, we use a model for the Imperial Valley from Fuis et al. (1984). In calculating the event-pair similarity, we required the cross-correlation coefficient to be at least 0.7 and the number of differential times to be at least 8.

Our method yields 2,282 detected events between 30 September to 11 October 2020, in comparison to only 1,711 events in the Southern California Seismic Network (SCSN) catalog (Hutton et al., 2010) during the same time interval (Figure S3 in Supporting Information S1). Among the detected events, 1,373 of these could be relocated precisely. The spatial distribution of relocated seismicity reveals a complex fault structure with a 162°-trending main fault and several en-echelon structures striking roughly perpendicular to the main fault (Figure 2). At depth >6.5 km (in the basement), the 162°-trending main fault shifts toward the North-South direction. These structures are consistent with the focal mechanisms from the SCSN catalog (Hutton et al., 2010). Our catalog does not include magnitudes since many of these events are small, and we cannot confidently estimate their magnitudes.

#### 3.2. GPS

This study utilizes daily and 5 min sampled GPS position time series in the International Terrestrial Reference Frame 2014 reference frame (Altamimi et al., 2016) preprocessed by Nevada Geodetic Laboratory using final orbit solutions (Blewitt et al., 2018). The original time series contains a transient geodetic signal at the time of the swarm and various other signals (seasonal variations, co-seismic steps, common mode jitter). To make use of these GPS data in studying the swarm, we need to separate the surface displacements related to the swarm from those resulting from other sources. The key steps are summarized here. Further details can be found in Text S1 in Supporting Information S1.

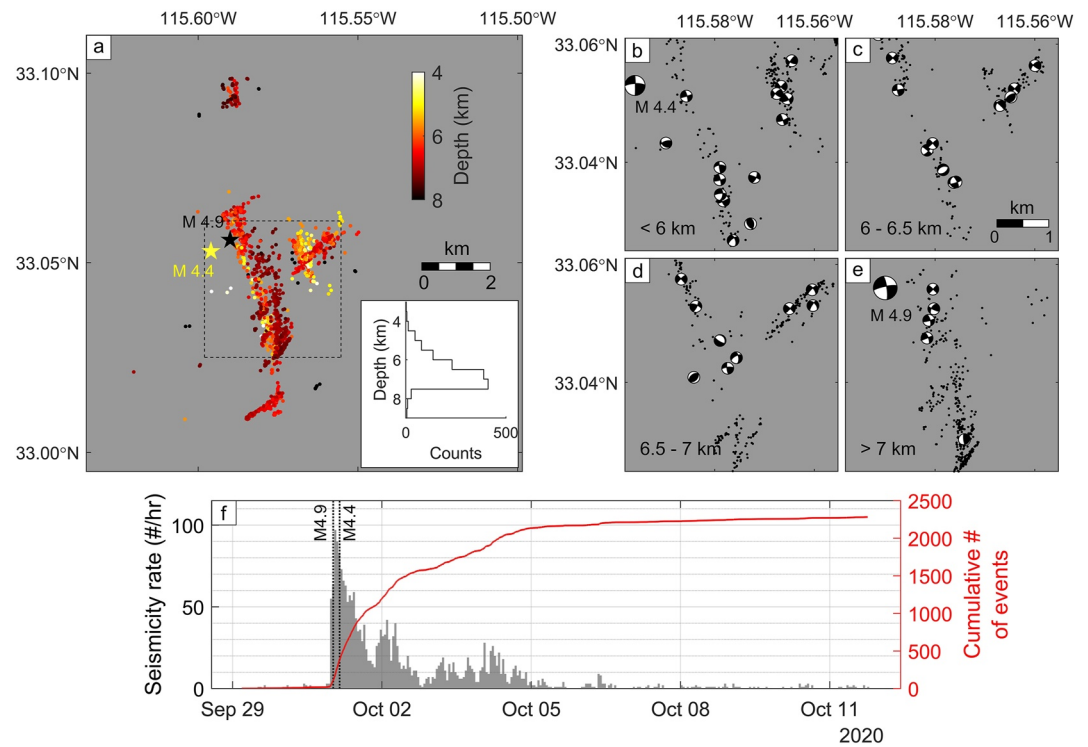


**Figure 2.** Seismicity catalog of the 2020 Westmorland swarm generated from this study (Siorattanakul et al., 2022). (a) Map view of 1,373 high-resolution relocated events color-coded by depth with a depth histogram as inset. The focal mechanisms are taken from the matching events in the Southern California Seismic Network (SCSN) catalog. We plot only those larger than  $M2.7$  using relocated locations for the different depth ranges: (b) shallower than 6 km, (c) between 6 and 6.5 km, (d) between 6.5 and 7 km, and (e) deeper than 7 km. Since the relocation technique used in this study relies on waveform similarity, which can be inaccurate for large events, we use locations from the SCSN catalog for events larger than  $M4$ . (f) Seismicity rate evolution of the entire catalog of 2,282 events generated from this study, including those detected but not relocated. Our catalog does not contain magnitudes.

We first work with daily position time series between 1 January 2016, and 25 November 2020, from 113 regional GPS stations (Figure S2 in Supporting Information S1). Using a trajectory model (Bevis & Brown, 2014), we remove the long-term linear trend and the co-seismic and instrumental steps (Table S1 in Supporting Information S1). Then, we extract the remaining nonlinear signals unrelated to the swarm, such as the seasonal signals and the common mode motion, using the modified variational Bayesian Independent Component Analysis (vbICA) decomposition (Gualandi et al., 2016), a blind source separation technique based on the original vbICA method (Choudrey & Roberts, 2003) but also takes into account data uncertainties and missing data (Chan et al., 2003) and has recently been successfully applied to daily sampled GPS position time series (e.g., Gualandi et al., 2020, 2017; Laroche et al., 2018; Michel et al., 2019; Serpelloni et al., 2018). Each isolated signal ( $i = 1, 2, \dots, R$ ) is an independent component (IC) which includes a stationary spatial function ( $U_{M \times R}$ ) explaining the relative amplitudes of the signals for the  $M$  different position time series ( $m = 1, 2, \dots, M$ ), the relative strength of the IC comparing to other ICs ( $S_{R \times R}$ ), and a time function ( $V_{T \times R}$ ) describing signals variation with time ( $t = 1, 2, \dots, T$ ). Since we first want to extract only the signals unrelated to the swarm, data points during the time of swarm (after 2020.732; 25 September 2020) from 34 stations within 45 km from the center of the Westmorland swarm are not used in the vbICA decomposition. We choose to decompose the signals unrelated to the swarm into 8 ICs (Figure S7 in Supporting Information S1) and they are all removed from the detrended position time series. We run the vbICA decomposition again, this time for the purpose of extracting deformations related to the swarm on a local-scale. Only the position time series near the time of the swarm between 2020.65 and 2020.81 (27 August to 24 October 2020) from 17 stations within 35 km from the center of the Westmorland swarm are used. We find that the first IC dominates and by itself explains over 77.2% of data variance (Figure S9 in Supporting Information S1). Therefore, we only keep this first IC and associate it with the swarm.

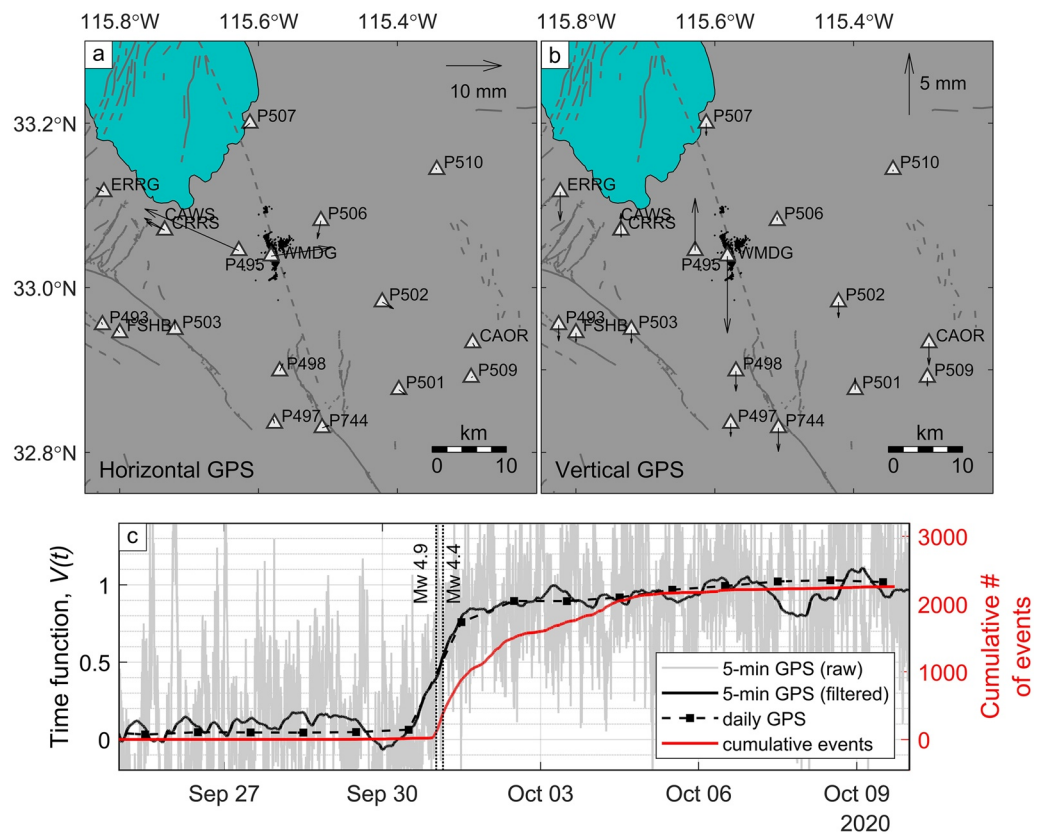


**Figure 3.** Extracted independent component (IC) related to the 2020 Westmorland swarm, which includes the spatial distribution (horizontal motion in (a) and vertical motion in (b)) and the associated time function (c). Unfiltered (gray) and filtered (black solid) time functions derived from 5 min Global Positioning System (GPS) position time series are compared with those derived from daily GPS position time series (black dashed) and the cumulative number of events (red). The filter used is a Savitzky-Golay 3rd order moving polynomial fit with a window of 50 hr (Savitzky & Golay, 1964). The hypocentral times of the two most significant earthquakes are shown as vertical dashed lines. The geodetic deformations due to these  $M4$  earthquakes are not removed. Compared to the noise levels of the 5 min GPS, these deformations are too small to be visible. Relocated seismicity from this study are shown as black dots in panels (a) and (b). Fault traces from the QFaults database (USGS, 2019) are shown as gray lines. The outline of the Salton Sea (cyan) is from Google Earth images (Google Earth V 7.3, 2020).

Since the extracted transient geodetic deformation started within 1 day from the onset of the swarm, it is not sufficient to use daily position time series to determine whether the geodetic deformation preceded the swarm or was coeval. We further improve the temporal resolution of our results by using the 5 min sampled position time series, also processed by the Nevada Geodetic Laboratory (Blewitt et al., 2018). Given larger uncertainties of the 5 min sampled position time series, directly performing vbICA decomposition does not provide the best possible result. Instead, we assert that the spatial function derived from the daily sampled position time series is generalizable to the 5 min sampled position time series and perform a projection to determine the associated time function with the 5 min temporal resolution. We further apply a low-pass Savitzky-Golay filter (Savitzky & Golay, 1964) based on a moving polynomial fit to mitigate high-frequency noises (Figure 3) and find a time lag of at least a few hours between the onset of geodetic deformation and seismicity. This filtering technique is non-causal and, therefore, does not temporally shift the onset of geodetic deformation. We further justify the choice of filter later in Section 5.4. We find the iterative GPS processing procedures presented here best suited for extracting the faint deformation related to the swarm. Raw and processed GPS time series at different processing steps from selected stations and vbICA components can be found in Figures S4–S11 in Supporting Information S1.

### 3.3. InSAR

To supplement the GPS measurements, we use the C-band Synthetic Aperture Radar (SAR) images acquired over the region by the Sentinel-1A satellite during September and October 2020. A total of five images between 9 September and 27 October 2020, from ascending track 166, frame 105, and 9 images between 3 September and 27 October 2020, from descending track 173, frame 480 were used. The original pixel size of the Sentinel-1 Single Look Complex (SLC) images generally ranges between 2–5 m, depending on the look angle of that pixel (see European Space Agency, 2014 for details). To reduce the spatial noise and estimate the coherence, all the SLC images are averaged by a factor of 30 and 6 along range and azimuth, respectively, resulting in multi-look imagery with a pixel size of 70 m by 84 m. Next, the multi-look images in each track are separately coregistered (Werner et al., 2000) to a single reference image, which is chosen to minimize the total spatiotemporal baseline. Six ascending and 20 descending interferograms are generated between all the possible pairs of SAR imagery acquired before and after the significant part of the swarm event (Table S3 in Supporting Information S1). The interferograms are then flattened using satellite ephemeris data and a Digital Elevation Model (DEM) with 90 m resolution provided by the Shuttle Radar Topography Mission (Farr et al., 2007) to remove the effects of a flat earth and surface topography (Franceschetti & Lanari, 1999). A 2-D phase unwrapping algorithm proposed by C. W. Chen and Zebker (2001) is used to recover the absolute values from ambiguous phase observations at the location of pixels with coherence above 0.80.

A set of wavelet-based filters are then used to remove the nuisance signal associated with various sources of error in the unwrapped interferograms. The effect of residual DEM error, which appears as a high-spatial-frequency noise, is reduced using a low-pass filter generated based on the Legendre polynomial wavelets (Shirzaei, 2013). This filter applies a hard thresholding operation to the high-pass sub-band (i.e., details components) of each decomposed unwrapped interferogram. The spatially correlated nuisance terms are mainly caused by the atmospheric delay and the orbital and satellite clock errors. To remove these errors, each unwrapped interferogram is decomposed into its high-pass and low-pass sub-bands using a two-dimensional multiresolution wavelet transformation (Mallat, 1989). The effect of orbital errors is removed by fitting a ramp to the average component (i.e., the high-pass sub-band) through a robust regression method (Shirzaei & Walter, 2011). The detail coefficients, on the other hand, are used to correct the interferogram for the phase contributions from the topography-correlated component of atmospheric delay. To this end, a multiresolution wavelet analysis is also applied to the DEM of the study area, and the correlation between the resulting detail coefficients and that of the interferogram is estimated. Next, the correlated coefficients are down-weighted and fed into an inverse wavelet transformation to reconstruct the corrected unwrapped interferogram (Shirzaei & Bürgmann, 2012). We further apply a Gaussian filter with a width of 7 km to each interferogram to isolate the remaining spatially correlated errors in the unwrapped interferograms (Hooper et al., 2007), which are mainly caused by the turbulent atmospheric delay.

The deformation at the location of each pixel in each of the flight directions is then estimated as the weighted average of the displacements measured by individual interferograms (i.e., stacking), where weight is determined by the calculated spatial coherence. To enable this, all the interferograms are first interpolated at the location of all the pixels that had a coherence of 0.80 in at least one of the interferograms (i.e., the union of pixels). The resulting Line-of-Sight (LOS) displacements for ascending and descending tracks are shown in Figure 4.

To make the inversion more computationally amenable, we apply an equation-based quadtree downsampling procedure (C. Wang et al., 2014) to reduce the number of surface deformation observations while maintaining the essential features. This procedure is similar to the quadtree downsampling (e.g., Jónsson et al., 2002) in that it starts with a regular grid and iteratively subdivides the grid cells. However, the criteria for the subdivision of cells are based on fault geometry and gradients of the observed displacements. We start by generating a coarse grid with 1 km spacing and calculating the Green's function using the semi-analytical solutions for a dislocation embedded in an elastic homogeneous half-space (Okada, 1985) at the four corner points of each grid cell. We then compute the largest Green's function differences ( $g_i$ ) and largest displacement gradients ( $d_i$ ) for all the grid cells. Next, we select the grids above the 50th percentile of  $g_i$  and above the 10th percentile of  $d_i$  and divide them into four quadrants. We repeat this procedure until we have at least 2,000 quadrants. Using this procedure on data points that are within 15 km from the center of the swarm, we end up with 2,590 cells. The location and displacement rate of the sample point associated with each quadrant is estimated as the average coordinates and LOS rates of the enclosed points, respectively.

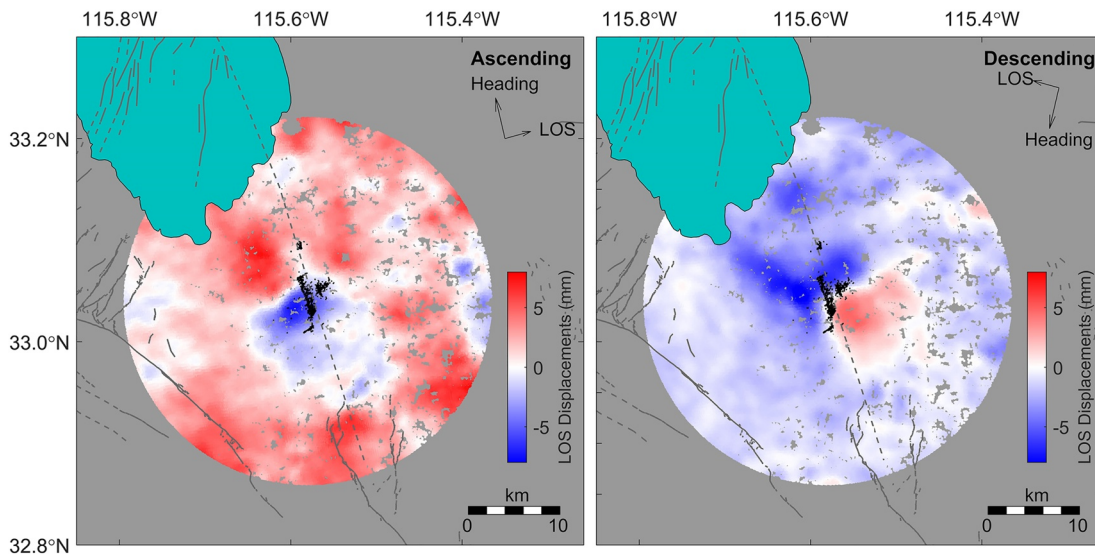


**Figure 4.** Interferometric Synthetic Aperture Radar (InSAR) Line-of-Sight (LOS) displacements from Sentinel-1A. The ascending LOS displacements (track 166, frame 105) include 5 images and 6 interferograms, while the descending LOS displacements (track 173, frame 480) include 9 images and 20 interferograms. Relocated seismicity from this study is shown as black dots. Fault traces from the QFaults database (USGS, 2019) are shown as gray lines. The outline of the Salton Sea (cyan) is from Google Earth images (Google Earth V 7.3, 2020).

### 3.4. Geodetic Slip Inversion

We use the observed cumulative surface displacements over the entire period of the swarm from both GPS and InSAR to invert for corresponding slip distribution at depth. Seismicity patterns and focal mechanisms (Figures 2a–2e and 5a–5c) suggest that the swarm occurred on a system of conjugate strike-slip faults dipping closely to vertical. We simplify this fault system with a fault model consisting of two orthogonal vertical faults. The fault model is meshed as  $1 \times 1$  km rectangular patches. The first fault (F1) is 22 patches long, 14 patches deep, and has a strike of  $162^\circ$ . The second fault (F2) is 16 patches long, 14 patches deep, and has a strike of  $72^\circ$  (Figures 6a–6c). The location and the strike of the two faults were chosen based on the discontinuity observed in the InSAR data. The faults extend beyond the significant features visible in the InSAR data and encompass the zone of observed seismicity.

Assuming an elastic homogenous medium, we can relate slip on the fault with ground deformations using the linear equation:

$$\vec{d} = \mathbf{G} \cdot \vec{m} \quad (1)$$

where  $\vec{d}$  is the data vector representing surface displacements at different spatial locations,  $\mathbf{G}$  is the Green's functions matrix computed from the semi-analytical solutions for a dislocation embedded in an elastic homogeneous half-space (Okada, 1985), and  $\vec{m}$  is the model input vector representing the amount of strike-slip and dip-slip on each fault patch. For InSAR data, the Green's functions are projected directly to the LOS displacements using the LOS unit vector at each pixel.

To include multiple data sets simultaneously, each data type  $i$  (horizontal GPS, vertical GPS, InSAR ascending, InSAR descending) is weighted by its variance (instrumental uncertainty squared,  $\sigma_i^2$ ). We further impose the Laplacian smoothing to prevent unreasonably large spatial variations in slips resulting from the tradeoffs between slips at the neighboring cells and zero-slip along all fault boundaries that are not the free surface. The Laplacian is calculated using a formulation from Huiskamp (1991) with 16 nearest neighbors. With these additional constraints, we now seek to minimize the following cost function  $\Phi(\vec{m})$  for a slip model  $\vec{m}$ :

$$\Phi(\vec{m}) = \left( \sum_{\text{all data types}} \frac{1}{\sigma_i^2} \|\mathbf{G}_i \cdot \vec{m} - \vec{d}_i\|_2^2 \right) + \frac{1}{\lambda} \|\Delta \vec{m}\|_2^2 \quad (2)$$

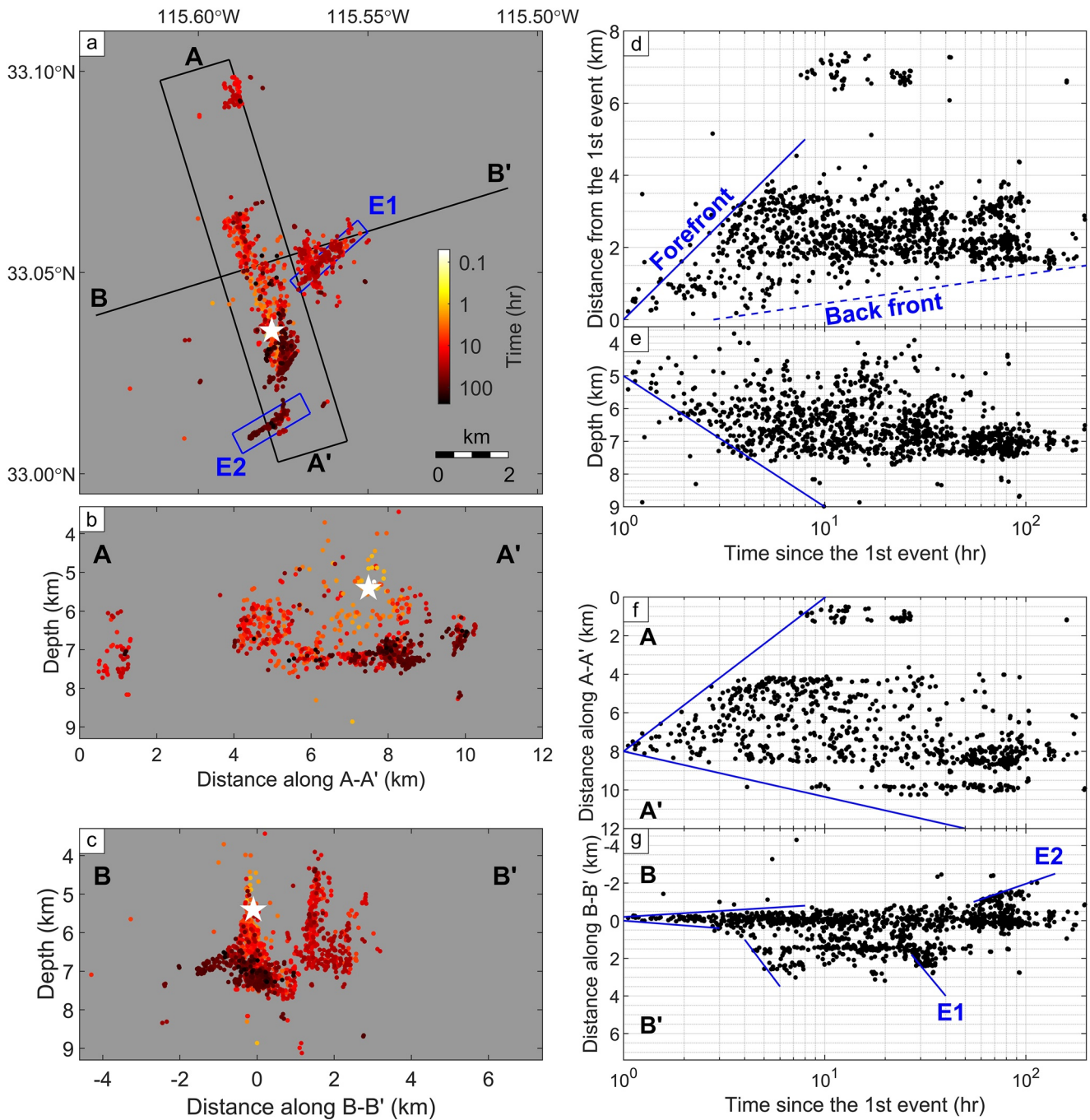


**Figure 5.** Spatio-temporal evolution of relocated seismicity generated from this study in (a) map view, (b) A-A', and (c) B-B' cross-sections color-coded by the logarithm of time since the first relocated event (white star). The complex behaviors of seismicity expansion are shown using (d) three-dimensional distance from the first relocated event, (e) depth distribution, (f) distance along A-A', and (g) distance along B-B'. Blue solid lines denote the various seismicity expansion fronts. In particular, the expansions of seismicity on the en-echelon structures E1 and E2 (blue boxes in panel (a)) are annotated in panel (g). The blue dashed line indicates seismicity back front marking the expansion of the zone of seismicity quiescence. For panels (b and f), only events within 1 km from the main fault (black box in panel (a)) are shown. Because the relocation technique used in this study relies on waveform similarity, a few larger events are excluded.

where  $\| \cdot \|_2$  is the L2-norm,  $\mathbf{\Delta}$  is the Laplacian matrix, and  $\lambda$  is the weight attributed to the Laplacian smoothing constraint. Zero-slip constraints can be imposed by forcing non-diagonal values in the Laplacian matrix corresponding to the boundary patches to zero. This minimization problem can be written as a system of linear equations and can be solved with a matrix inversion.

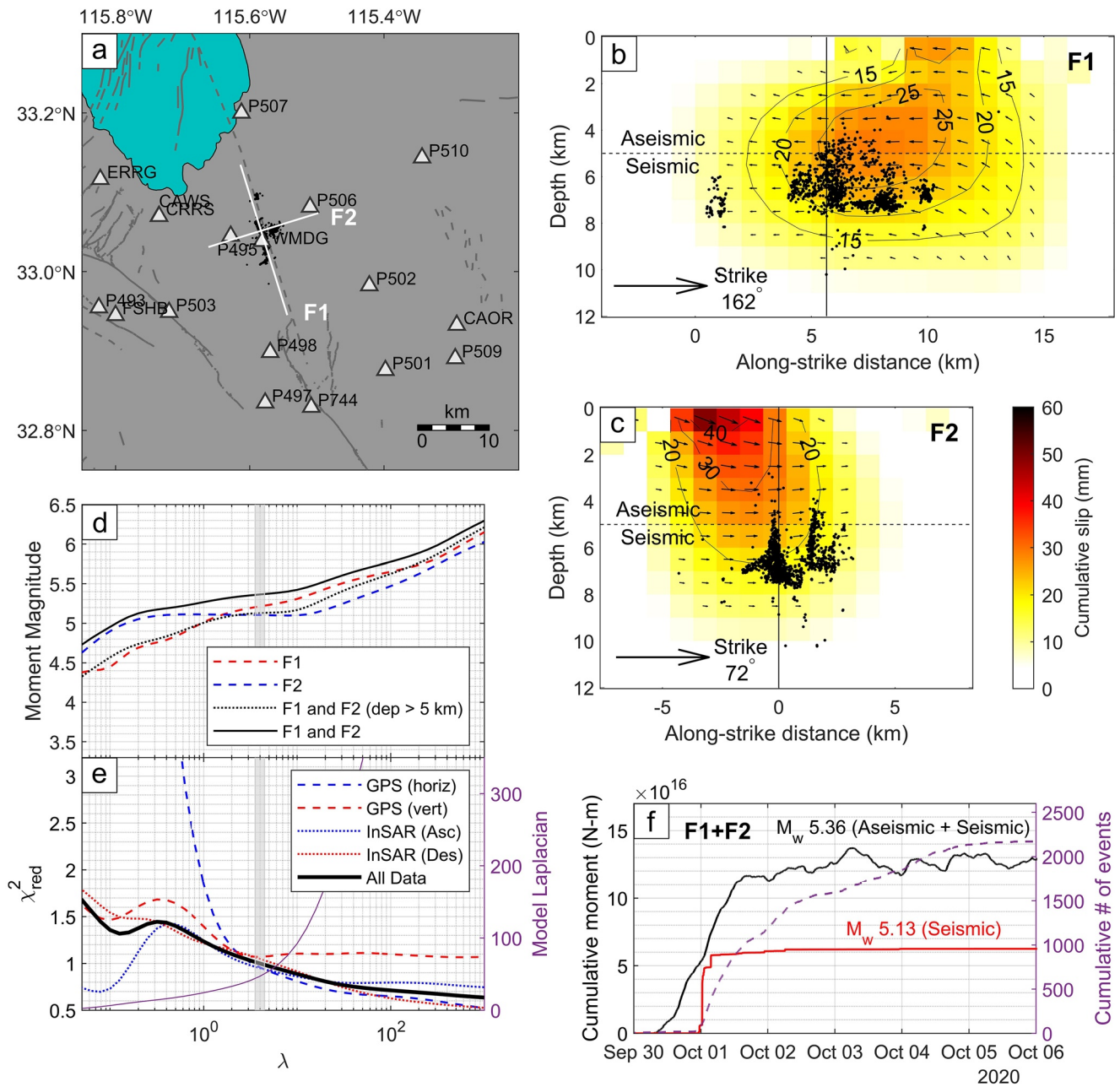


**Figure 6.** Geodetic slip inversion. (a) Location of the fault planes (white lines) and the GPS stations (black triangles) used in the inversion. Cumulative slip over the swarm duration along (b) F1 and (c) F2 from the preferred slip model. The intersection of F1 and F2 (black vertical lines), the inferred aseismic-seismic depth boundary (black horizontal dashed lines), and the relocated seismicity from this study (black dots) are shown in panels (b) and (c). (d) Moment and (e) reduced chi-square as a function of smoothing parameter  $\lambda$ . The preferred model uses  $\lambda = 10^{0.6}$  (gray bar). (f) The time evolution of cumulative moment release from the geodetic inversion (black, filtered with the Savitzky-Golay filter (Savitzky & Golay, 1964) similar to Figure 3c), which reflects both the aseismic and seismic processes, and the cumulative seismic moment (red) calculated using magnitudes from the Southern California Seismic Network (SCSN) catalog (Hutton et al., 2010). The slip model is stationary but evolves according to the cumulative geodetic moment.

We explore the range of possible slip models by varying the Laplacian weight  $\lambda$  and compare the tradeoff between the smoothness of the slip model and the misfit between the forward model and the data using the  $L$ -curve criterion (Hansen, 1992). Additionally, we further evaluate the reduced chi-square for each data type  $i$ , defined as follow:

$$\chi_{red,i}^2(\bar{\mathbf{m}}) = \frac{1}{n\sigma_i^2} \|\mathbf{G}_i \cdot \bar{\mathbf{m}} - \bar{\mathbf{d}}_i\|_2^2 \quad (3)$$

**Table 1**

*Data Uncertainty ( $\sigma_i$ ) and Reduced Chi-Square Statistics of the Misfit Between Observations and the Forward Prediction of Ground Deformations ( $\chi_{red}^2$ ) Calculated Using the Preferred Slip Model After Normalization of the Data Uncertainties (Figures 6b and 6c)*

Data type	Uncertainty, $\sigma_i$	Reduced chi-square, $\chi_{red}^2$
GPS (horizontal)	0.4 mm	0.96
GPS (vertical)	1.5 mm	1.07
InSAR (ascending)	2.9 mm	0.95
InSAR (descending)	2.1 mm	1.05
Combined	N/A	1.00

where  $n$  is the number of data points for data type  $i$ . The most appropriate model that does not overfit or underfit would have a reduced chi-square of one for every individual data type. To properly account for errors in the a priori estimates of data uncertainties, the geodetic inversion is performed iteratively, similar to the scheme adopted by Thomas et al. (2014). In the first inversion, data uncertainty for all data types is assumed to be one. Afterward, the data uncertainty for each data type is renormalized so that the corresponding reduced chi-square for that data type is equal to one. The subsequent inversion is then performed using the updated data uncertainties. After a few iterations, the slip inversion should produce a reduced chi-square that converges to one.

## 4. Kinematics of the 2020 Westmorland Swarm

### 4.1. Spatio-Temporal Evolution of Seismicity

Our high-resolution seismicity catalog reveals the swarm's complex migratory behaviors (Figure 5 and Movies S1–S3). A cluster of  $\sim 10$  seismic events at 4.5–5.5 km depth (Figure S12 in Supporting Information S1) were detected  $\sim 10$  hr before the main swarm activity, which started on 30 September 2020, at 21:57 UTC. The overall pattern can be described by an expansion of seismicity forefront and back front, with sustained seismic activity in between lasting  $\sim 140$  hr (Figure 5d). Both fronts expanded nonlinearly with a rapid onset followed by decaying expansion rates, which we discuss more in Sections 5.3 and 5.7.

Figure 5 shows the detailed spatio-temporal evolution of the swarm. During the first 20 hr, the swarm expanded logarithmically along the main  $162^\circ$ -trending vertical fault zone, roughly 500 m wide. The expansion was asymmetric, with a dominant northward along-strike propagation. The along-dip expansion terminated at  $\sim 8$  km. Coincident with the expansion along the main fault, two adjacent 500 m wide steeply dipping structures parallel to the main fault forming a flower structure were reactivated  $\sim 4$  hr after the swarm activity started. Later at 25 and 55 hr, en-echelon structures perpendicular to the main fault (structures E1 and E2 in blue boxes of Figure 5a, respectively) were reactivated. Seismicity on these en-echelon structures was localized along narrow zones no more than 200 m wide at a depth of  $\sim 6.5$  km or deeper, coinciding with the basement. Compared to the swarm duration, the reactivations were short-lived and exhibited a nonlinear migration front (blue lines annotated with E1 and E2 in Figure 5g). We also observed a seismicity gap between latitude  $33.07^\circ$ – $33.09^\circ$ N that could be related to the heterogeneity of stresses on the fault. All large earthquakes with  $M > 4$ , including the largest  $M_w$  4.93 event, were within the first 6 hr of the swarm, and they did not appear to cause any significant changes in the seismicity rate (Figure S12 in Supporting Information S1). This could be partly due to catalog incompleteness in the early period after large events (e.g., Hainzl, 2016).

### 4.2. Time-Dependent Geodetic Slip Model

The linear decomposition of the signal into a limited number of components, whether using a PCA or an ICA, makes it very effective for carrying out an inversion of the time evolution of slip (Kositsky & Avouac, 2010). Instead of epoch-by-epoch inversions, we can perform inversions for only the spatial functions associated with each component ( $U_{M \times r}$ ), where  $r$  refers to a set of all components representing the geodetic transient of interest. The time evolution of slip is obtained by multiplying the slip models resulting from these inversions by  $S_{r \times r} V_{r \times T}^T$  (see Kositsky & Avouac, 2010 for details). Since only one component related to the swarm sequence was extracted, our resulting model is stationary in space with cumulative moment varying according to the time function  $V(t)$  retrieved from the vbICA decomposition (Figure 3). Our preferred model (Figure 6) uses a Laplacian weight of  $10^{0.6}$ , which yields the best trade-off between data fitting and the smoothness of the solution (Figure 6e and Figure S13 in Supporting Information S1). Although the details of slip distribution would vary if we were to choose a different Laplacian weight, the total moment release is relatively well-constrained at  $M_w$  5.3–5.4 (Figure 6d). The uncertainties assigned to each data set following our iterative inversion (Section 3.4) are reported in Table 1. After only one iteration, the reduced chi-square for each data type gets close to unity within 7% (Table 1). Therefore, no further iteration was deemed necessary. Further analysis on the sensitivity

of the results to the assumed fault geometries, checkerboard resolution test (Lévêque et al., 1993), and variances estimation with jackknife test (Efron & Stein, 1981) are provided in Text S2 and Figures S14–S17 in Supporting Information S1.

Our slip model reveals conjugate faulting with right-lateral strike-slip motion along the 162°-striking main fault F1 and left-lateral strike-slip motion along 72°-strike orthogonal fault F2 with peak slip occurring along F2 near the surface (Figure 6). To determine the slip modes observed, we compare the geodetically resolved moment with the seismic moment. Since we do not calculate magnitudes for our seismicity catalog, we use magnitudes from the SCSN catalog. The additional events in our enhanced catalog are small and contribute only a small fraction to the total seismic moment. We find that the relative contribution of the seismic and aseismic moment vary systematically with depth. For the depth range of seismicity (5–10 km), the geodetically resolved slip is equivalent to  $M_w$  5.13, roughly equal to the total moment release estimated from the seismicity itself. This suggests that the slip mode for this depth range is predominantly seismic. On the contrary, since there is only little seismicity above a depth of 5 km, the shallow slipping region on F2 must be mostly aseismic. Cumulatively over the entire swarm period, the aseismic moment release ( $M_w$  5.19) is ~20% larger than the seismic moment release ( $M_w$  5.13).

The predicted displacements from our preferred slip model show large misfits to the InSAR data close to the faults suggesting that the fault zone is complex and cannot be modeled perfectly with simple planar shear faults (Figure 7). The en-echelon step-over fault structures, prominent dilatational motion in this region (Crowell et al., 2013), plastic deformation, and inhomogeneity of elastic moduli could contribute to these misfits. However, we did not try to refine the model further because we are chiefly interested in the effect of the aseismic processes on the evolution of the swarm. Furthermore, the seismicity occurred in the basement, at ~5 km distance from the peak aseismic slip, and stress changes there are not very sensitive to the detail of the source near the surface.

GPS position time series with sub-daily resolution resolves that the onset of geodetic deformation preceded the onset of seismicity by at least a few hours (Figures 3 and 6f). This suggests that fault slip in the early period was aseismic. Moreover, since the moment release at depth >5 km is related predominantly to seismicity, the slow slip event was probably initiated in the shallow portion of F2, where aseismic slip was the highest. Although it seems reasonable at this point to conclude that the slow slip event triggered the swarm sequence, proximity in space and time does not require a causal relationship. We explore further the relationship between the slow slip event and the swarm sequence using triggering analysis and a stress-driven model in Section 5. We also note that most geodetic moment releases terminated ~1 day after the swarm began (Figure 6f). However, seismicity continued for ~5 more days, suggesting a secondary mechanism other than the slow slip event that drove the latter part of the swarm.

## 5. Modeling the 2020 Westmorland Swarm

The seismic and geodetic observations of the 2020 Westmorland swarm provide a unique opportunity to study the mechanics of the swarm in detail. This section discusses the interplays of the processes driving the swarm (the slow slip event, inter-earthquake static stress triggering, and pore pressure diffusion) and quantifies their relative contributions in driving the seismicity. We first show that the swarm was driven by the slow slip event rather than a result of cascade triggering using static stress transfer (Sections 5.1–5.3). Next, we model the temporal evolution of seismicity during the swarm sequence using stress changes from the slow slip event and a stress-driven model based on rate-and-state friction (Sections 5.4–5.6). Then, we associate the unexplained seismicity with pore pressure diffusion, which helps sustain the swarm sequence (Section 5.7). Finally, our models provide constraints on the friction parameter and pore pressure, which we compare with values independently derived from the responses of seismicity to hydrological cycles and solid Earth tides (Section 5.8).

### 5.1. Aseismic Slip Driven Vs. Cascading Failures

Two end-member scenarios explaining the spatial and temporal evolution of the swarm can be envisioned. The first scenario postulates that the earthquakes are driven only by external forcings, such as the slow slip event, through Coulomb Failure Stress changes (dCFS) with minimal interactions between the earthquakes themselves. This scenario is similar to Dieterich's model of aftershocks (Dieterich, 1994), which assumes that all aftershocks are directly triggered by a single mainshock. The second scenario postulates that an earthquake produces earthquakes resulting in a series of cascading events (Ellsworth & Beroza, 1995). To distinguish which of these

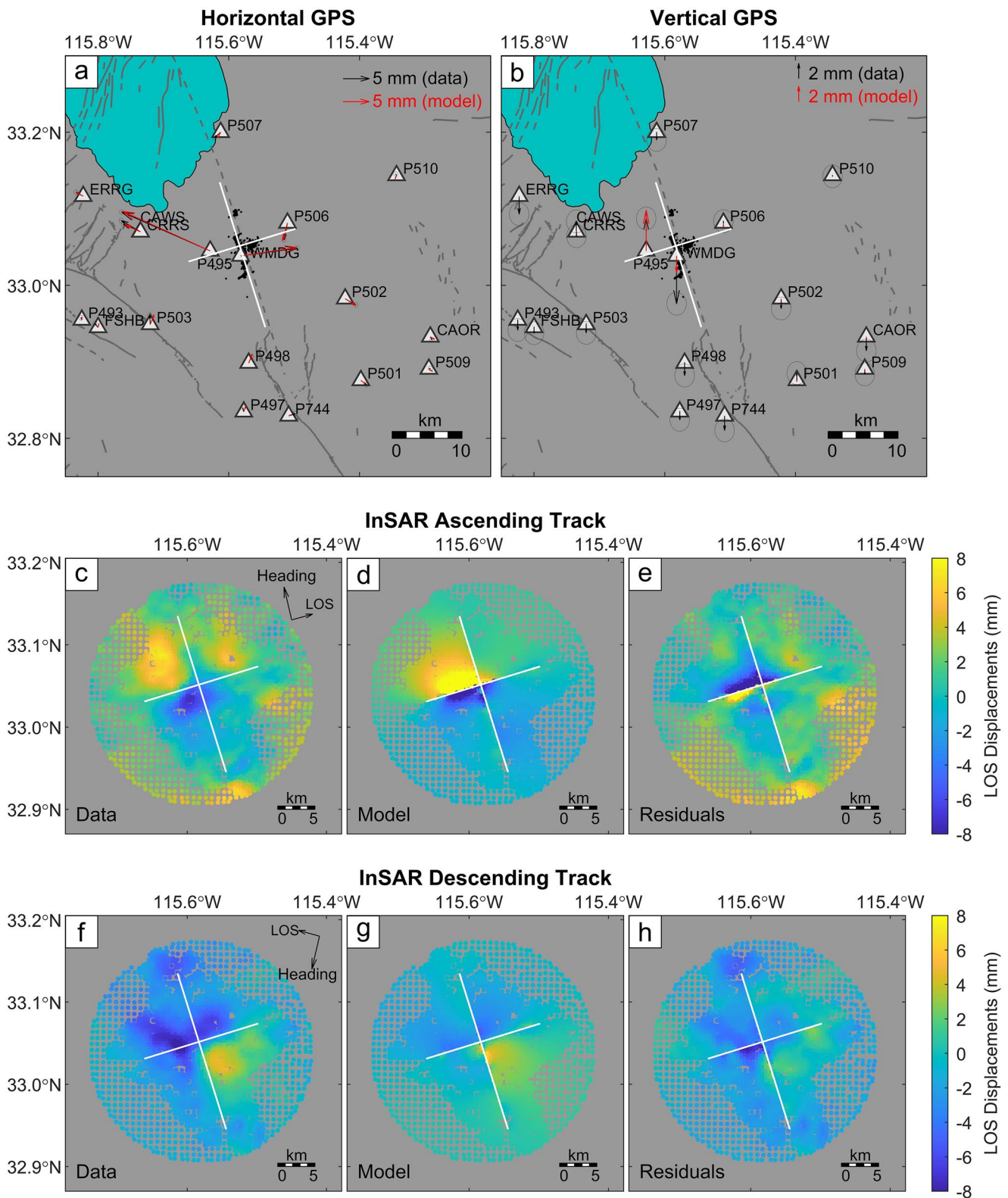


**Figure 7.** Comparison of the observed and predicted values from our preferred slip model for (a) horizontal and (b) vertical GPS displacements. (c) Observed values, (d) predicted values, and (e) the residuals for InSAR ascending track. (f) Observed values, (g) predicted values, and (h) the residuals for InSAR descending track. The location of the fault planes is shown as white lines.

mechanisms is dominant, we compute and compare dCFS induced on each seismic event by the slow slip event and by all earthquakes preceding it to investigate which of these two end-member scenarios is more likely. The hydrothermal setting of Westmorland, California, suggests that the presence of fluids must be accounted for. All dCFS calculations in this study assume a friction coefficient of 0.4, chosen to account approximately for the effect of a hydrostatic pore pressure as is customary in such studies (King et al., 1994).

The computation of dCFS requires knowledge of the receiver's fault plane. Since we did not specifically determine focal mechanisms for this study, we restrict the analysis to 562 events with reported SCSN focal mechanisms. This is valid because large events, which dominate the stress transfer, are those with focal mechanisms. For each event, the fault plane is chosen to be the nodal plane from the focal mechanism that maximizes dCFS induced by each end-member scenario. For scenario 2 of cascade triggering, since the fault plane of the current event depends on dCFS from previous events and hence their fault planes which depend on all events before it, errors from previous calculations would stack up rapidly. To prevent erroneous results from staggering uncertainties, given that geodetically resolved slips at seismogenic depths are mostly constrained on F1, we further assert that the fault planes of the first event and largest  $M4.9$  event are the nodal planes closer to right-lateral strike-slip motion along F1. Concerning locations, we use the relocated locations from this study except for those with  $M > 4$  in which we use the locations from the SCSN catalog because we find their relocated locations inaccurate due to the dissimilarity of the waveforms with other small events in the catalog.

Besides the receiver's fault planes, we also need to know the properties of the sources. For scenario 1 of slow slip driven, since aseismic slip dominates the shallower parts of the faults (depth  $< 5$  km) while seismicity dominates the deeper parts (depth  $> 5$  km), the slow-slip source is taken to be the top 5 km of the geodetic slip model. However, instead of temporally evolving the slips according to the cumulative geodetic moment, we use the cumulative aseismic moment, calculated by subtracting the cumulative seismic moment (magnitudes from SCSN catalog) from the unfiltered cumulative geodetic moment and then filtered with the 3rd order Savitzky-Golay filter with 50 hr window. For scenario 2 of cascade triggering, since we need focal mechanisms to determine the source properties, we restrict the dCFS sources to only events with SCSN focal mechanisms. We approximate the earthquake source as a circular crack with a uniform stress drop  $\Delta\sigma$  assumed to be 0.1 MPa, consistent with other regional earthquakes in the Brawley Seismic Zone (Chen & Shearer, 2011; Hauksson, 2015), and the mean Coulomb stress drop of our geodetic model (Figure S18 in Supporting Information S1) estimated using a formulation based on energy considerations (Noda et al., 2013). Using stress drop and SCSN magnitudes, we estimate the slipping area  $A$  and the amount of slip  $D$  using the scaling relation  $M_0 \sim \Delta\sigma A^{3/2}$  (Kanamori & Anderson, 1975) and the definition of seismic moment  $M_0 = \mu AD$  along with the assumed crustal shear modulus  $\mu \sim 30$  GPa. For simplicity in calculation, we further approximate the circular rupture as a square of equal area and use semi-analytical solutions in an elastic half-space to calculate dCFS (Okada, 1992). For a given event, the dCFS are calculated using all events before it as sources, not just from the most recent event.

Using the outlined procedures, we find that dCFS induced on each seismic event by the slow slip event is generally larger than those induced by all preceding earthquakes (Figure 8). This holds even for scenario 2, where the fault planes were chosen to be more favorable for cascade triggering. We find that up to 68% of events could be driven by the slow slip event, with the median dCFS of 22 kPa (Figure 8a). About 22%–35% of events can be attributed to inter-earthquake static stress triggering. The remaining 9%–14% of events have negative dCFS and are neither encouraged by the slow slip event nor cascade triggering, requiring a third mechanism.

Since stress drops for each event can vary over a few orders of magnitude, we further investigate the sensitivity of our analysis to the assumed stress drop of 0.1 MPa. We find a systematic trend with more events likely triggered by the slow slip event for lower stress drop. For the stress drop  $\Delta\sigma$  ranging from 0.1 to 3 MPa, at least 44% of events are encouraged by the slow slip event when choosing the fault planes based on scenario 1 of slow slip driven and 35% of events for scenario 2 of cascade triggering (Figure S19 in Supporting Information S1). We acknowledge that the uncertainty in the estimate of dCFS due to errors in hypocentral locations and focal mechanisms could bias the analysis toward underestimating the performance of the cascade model (Hainzl et al., 2012).

## 5.2. Faulting Type of Seismic Events

Our high-resolution seismicity catalog reveals the fault zone structure but not the faulting type of each structure. Since dCFS induced at each event by the slow slip event is generally larger than dCFS induced by all earthquakes

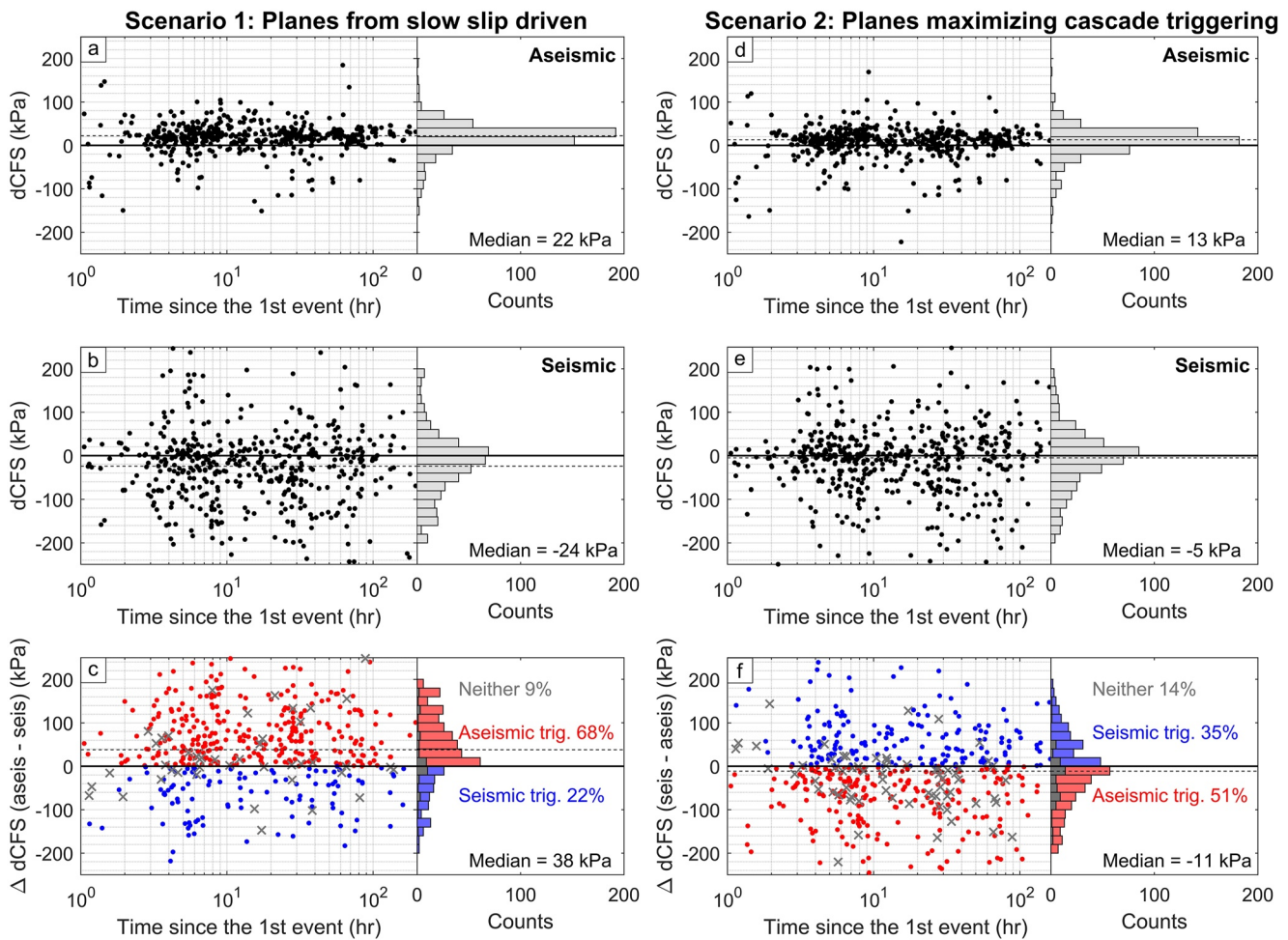


**Figure 8.** Coulomb Failure Stress changes (dCFS) at relocated events from this study with matching SCSN focal mechanisms. In scenario 1, failure planes are the nodal planes with larger dCFS induced by the slow slip event. With such nodal planes, the distribution of dCFS induced by (a) the slow slip event, (b) all preceding earthquakes, and (c) their differences are shown. In scenario 2, failure planes are the nodal planes with larger dCFS induced by all preceding earthquakes. With such nodal planes, the distribution of dCFS induced by (d) the slow slip event, (e) all preceding earthquakes, and (f) their differences are shown. The median value for each distribution is plotted as a horizontal dashed line. Based on the larger dCFS values, we can classify the events into different categories, whether they are likely triggered by the slow slip event, other seismic events, or encouraged by neither, because dCFS values are negative (gray crosses in panels (c) and (f)).

preceding it (Section 5.1), we assert that the nodal planes with larger dCFS induced by the slow slip event are the true fault planes (Scenario 1) and their associated rakes describe the faulting type. From the 437 relocated events from this study with matching SCSN focal mechanisms that are in the region with positive dCFS induced by the slow slip event (Figure 9c), we classify 85 events as right-lateral strike-slip, 269 events as left-lateral strike-slip, 55 events as normal faulting, and 28 events as reverse faulting (Figure 9). Even though only 19% of events have right-lateral strike-slip motion, they include most large events on the 162°-striking main fault F1 and makeup 94% of the total seismic moment release. The remaining seismic moment release is accommodated by primarily left-lateral strike-slip events on the en-echelon structures orthogonal to the main fault F1. Normal and reverse faulting accounts for <1% of the total seismic moment release. The relative ratio between the different faulting types does not significantly change with time (Figure S20 in Supporting Information S1). The distribution of fault planes selected to favor cascade triggering (scenario 2) is shown in Figures S21–S22 in Supporting Information S1.

### 5.3. Logarithmic Expansion of Seismicity Controlled by the Slow Slip Event

Our high-resolution relocated seismicity catalog reveals that seismicity during the swarm expanded nonlinearly with a rapid onset followed by decaying expansion rates (Figure 6d). The insufficient spatial resolution of the

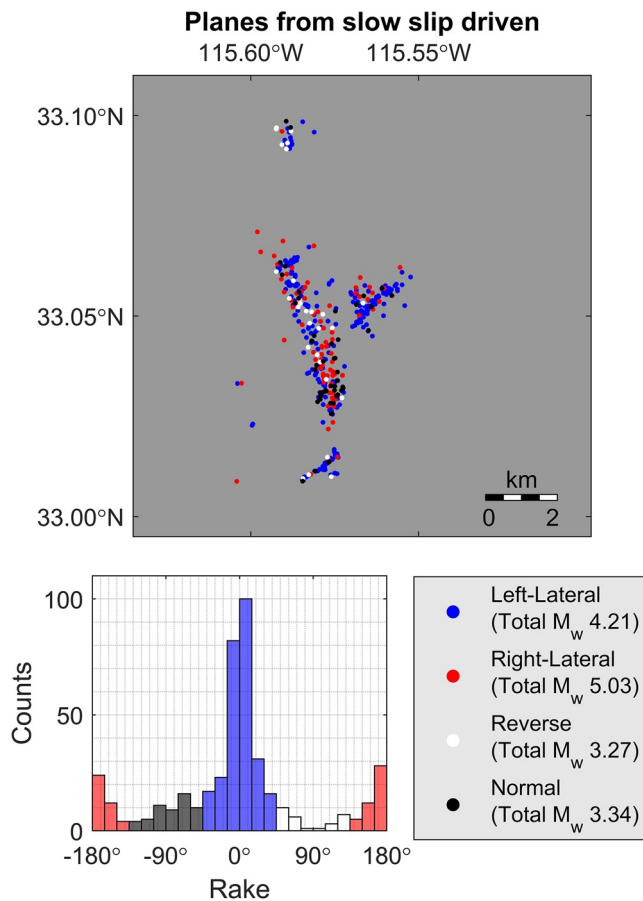


**Figure 9.** Map of relocated events from this study with matching Southern California Seismic Network (SCSN) focal mechanisms color-coded by faulting type and a histogram of the corresponding rake. The faulting types are chosen from the nodal planes with larger dCFS induced by the slow slip event (scenario 1 in Figure 8). Only those with positive dCFS are considered.

non-relocated catalog could make these fronts appear to expand linearly. To further distinguish whether the expansion is  $\sqrt{t}$  or  $\log(t)$  from the observed seismicity is extremely difficult since envelopes of seismicity are not precisely defined (Figure S23 in Supporting Information S1), though we think that  $\log(t)$  expansion is more likely due to different reasons. First, describing seismicity front as  $\sqrt{t}$  expansion would require hydraulic diffusivity of  $100 \text{ m}^2/\text{s}$ , which is outside of a commonly accepted range for fluid-driven swarms (e.g., Amezawa et al., 2021). Cascading earthquakes can also lead to an apparent diffusive expansion of the seismicity (Helmstetter & Sornette, 2002a), but this is unlikely because static stress triggering (Section 5.1) and statistics of times between earthquakes (Section 5.5) suggest that earthquakes are predominantly non-interacting. Second, the slow slip event began abruptly, followed by a decaying slip rate, which can be reasonably modeled using an exponential decay or a logarithmic function typically used for afterslip (Ingleby & Wright, 2017). Earthquakes driven by afterslip are expected to expand as  $\log(t)$  (Perfettini et al., 2018), as observed in selected case studies (e.g., Frank et al., 2017; Kato & Obara, 2014; Peng & Zhao, 2009; Tang et al., 2014).

To further investigate the possibility of the slow slip event controlling the expansion of the seismicity front, we evaluate the time evolution of dCFS induced by the slow slip event (top 5 km of the geodetic slip model) along the main fault plane F1. The time evolution of the slow slip event is assumed to be proportional to the time evolution of the aseismic moment calculated by subtracting cumulative seismic moment (magnitudes from SCSN catalog) from the unfiltered total geodetic moment and then filtered with the 3rd order Savitzky-Golay filter with 50 hr window, similar to what we used previously in Section 5.1. We calculate dCFS for both the right-lateral strike-slip plane F1 and the left-lateral strike-slip plane F2 to include events on en-echelon structures and retain the maximum value at each gridded point (Figures 10a and 10b). We assert that a certain threshold of dCFS is needed to nucleate a seismic event and track the expansion of the different dCFS contours along F1. The results reveal that the contours expanded nonlinearly, roughly parallel to the observed seismicity front (relocated catalog from this study), with rapid onset followed by a decaying expansion rate (Figures 10c and 10d and Supporting Movie S4). The average dCFS required to trigger seismicity is

estimated to be  $\sim 30 \text{ kPa}$ , similar to the median dCFS value of  $22 \text{ kPa}$  required to trigger seismicity estimated in Section 5.1 (Figure 8a). Regardless of which dCFS contour we pick, there is a time lag between the stress changes and the observed seismicity, highlighting a finite nucleation time consistent with earthquake nucleation models based on laboratory friction laws (e.g., Dieterich, 1994).

#### 5.4. Seismicity Rate Evolution From a Stress-Driven Model

We have shown in Section 5.3 that stress changes due to the slow slip event can explain the rapid expansion of the seismicity front. Here, we further investigate the possibility of quantitatively explaining the time evolution of seismicity rate using a stress-driven model based on one degree of freedom spring-slider system close to failure (Dieterich, 1994; Heimisson & Segall, 2018), hereafter referred to as “Dieterich’s model.” The friction coefficient  $\mu$  in this model evolves with slip velocity  $V$  and a state variable  $\theta$  according to the rate-and-state formulation derived from laboratory experiments sliding two rock surfaces or gouge layer (Dieterich, 1979, 1981; Ruina, 1983; see Marone, 1998 for review). Dieterich’s model further uses an approximation that the product of slip velocity  $V$  and the state variable  $\theta$  is large compared to the critical slip distance  $D_{RS}$ , that is,  $V\theta/D_{RS} \gg 1$ , and assumes that the friction parameter  $a$  describing material resistance to an increase in slip velocity ( $\partial\mu/\partial(\ln V)$ ) and initial

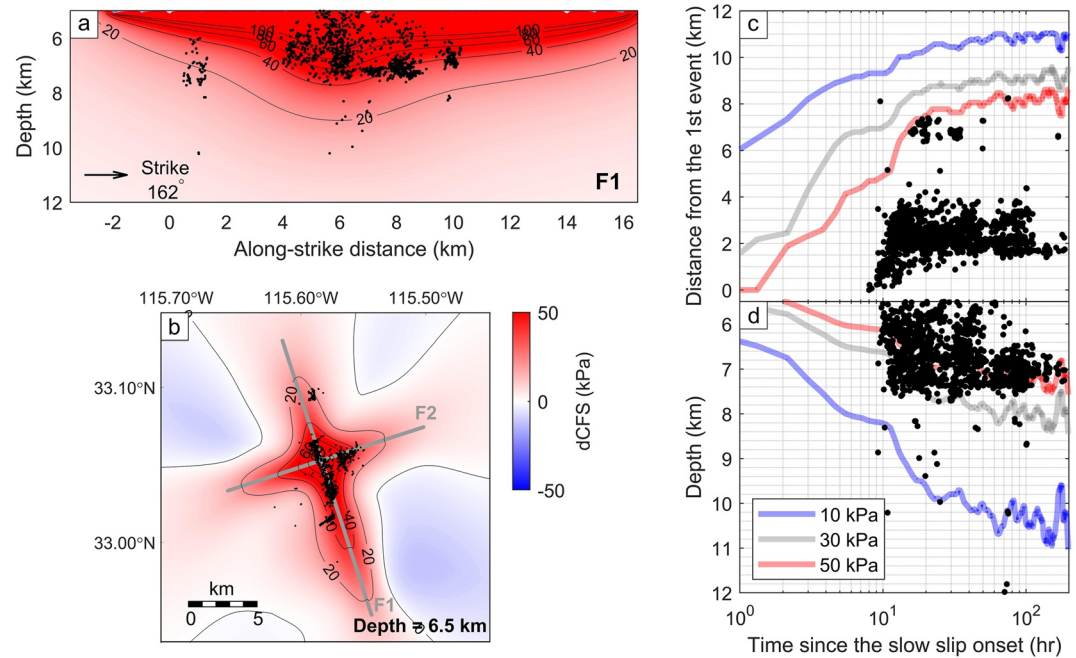


**Figure 10.** dCFS induced by the slow slip event calculated (a) on F1 and (b) at a depth layer of 6.5 km. The values displayed are the maximum assuming either the right-lateral strike-slip plane F1 or left-lateral strike-slip plane F2 as the failure plane. Time evolution of (c) the maximum distance between the contours of different dCFS values on F1 (panel (a)) and the first relocated event and (d) the depth extent of the same contours. Relocated seismicity from this study is shown as black dots. The onset of the slow slip event is picked to be  $\sim 8$  hr before the start of the swarm.

effective normal stress  $\sigma$  are uniform. The seismicity rate  $R(t)$  on a fault would then respond to an evolving shear stress perturbation  $\Delta\tau(t)$  according to the following equation (Dieterich, 1994; Heimisson & Segall, 2018):

$$\frac{R(t)}{r} = \frac{e^{\Delta\tau(t)/a\sigma}}{1 + \frac{1}{t_a} \int_0^t e^{\Delta\tau(x)/a\sigma} dx} \quad (4)$$

where  $t_a = a\sigma/\dot{\tau}_a$  is the characteristic aftershock decay time for returning to steady-state, and  $r$  is the background seismicity rate corresponding to a constant background stressing rate  $\dot{\tau}_a$  prior to the perturbation. When normal stress changes are small relative to the effective normal stress  $\sigma$ , we can substitute shear stress changes  $\Delta\tau(t)$  with the cumulative Coulomb Failure Stress changes  $dCFS(t)$ , which we use throughout our study (Dieterich et al., 2000; Heimisson & Segall, 2018). Because the slip rate during the slow slip event is of a few mm/day, value orders of magnitude larger than the mm/year geological slip rate associated with tectonic loading, we do not consider background tectonic stressing in the stress changes term.

We further simplify the analysis by treating the observed seismicity as a point process and do not consider spatial information. All detected events in our catalog, including those not relocated, are used. The background seismicity rate  $r$  prior to the swarm is estimated from the SCSN catalog (Figure S24 in Supporting Information S1) and then rescaled to our catalog using the total number of detected events  $N$  during the swarm, that is,  $r_{our\ catalog} = r_{SCSN} \cdot N_{our\ catalog} / N_{SCSN}$ . Since our slip model is stationary, if the medium is assumed to be homogeneous,  $\Delta\tau(t)$  is proportional to the cumulative moment release. We are left with only two fitting constants, the decay time  $t_a$  and the proportionality constant  $\Delta\tau_0/a\sigma$  between  $\Delta\tau(t)/a\sigma$  and the normalized cumulative moment release, where  $\Delta\tau_0 = \Delta\tau(t = \infty)$  is the cumulative dCFS over the swarm duration. A set of sensitivity tests (Figure S25 in Supporting Information S1) show that  $\Delta\tau_0/a\sigma$  controls the amount of time lag between the slow slip event and seismicity while  $t_a$  controls the maximum seismicity rate.

Even though Dieterich's model assumes no interactions between sources, we can approximately account for it by including dCFS induced by the earthquakes themselves in the driving shear stress, such as those done in the

numerical models of Ziv and Rubin (2003). Theoretically, this is valid if magnitude statistics are not altered by stress perturbations (Heimisson, 2019). To assess whether the inter-earthquake static stress transfer plays a vital role in driving the swarm, we model the seismicity rate using both the stress changes from only the slow slip event (left panels in Figures 11 and 12) and the stress changes from the total geodetically resolved slip which includes also slips due to earthquakes (right panels in Figures 11 and 12). Similar to Sections 5.1 and 5.3, the cumulative aseismic moment used here is derived by subtracting the cumulative seismic moment (magnitudes from the SCSN catalog) from the unfiltered cumulative geodetic moment. Since Dieterich's model is highly nonlinear and hence affected by the high-frequency noises, we compare three different methods to denoise the cumulative moment:

1. fitting with a Heaviside step function  $H(t - t_0)$ , representing an instantaneous deformation end-member (Figure S26 in Supporting Information S1),
2. fitting with an exponential function  $H(t - t_0) \cdot A_{exp} \left( 1 - e^{-(t-t_0)/\tau_{exp}} \right)$ , representing a continuous deformation (Figure 11), and
3. applying a Savitzky-Golay filter based on moving polynomial to remove high-frequency noises (Figure 12)

Model fitting is done using a standard grid search to minimize the root-mean-squared error (RMSE). Given that most of the geodetic moment release already terminated  $\sim 1$  day after the start of the swarm, attempting to fit the model with the seismicity rate from the entire swarm duration leads to a significant underestimation of peak

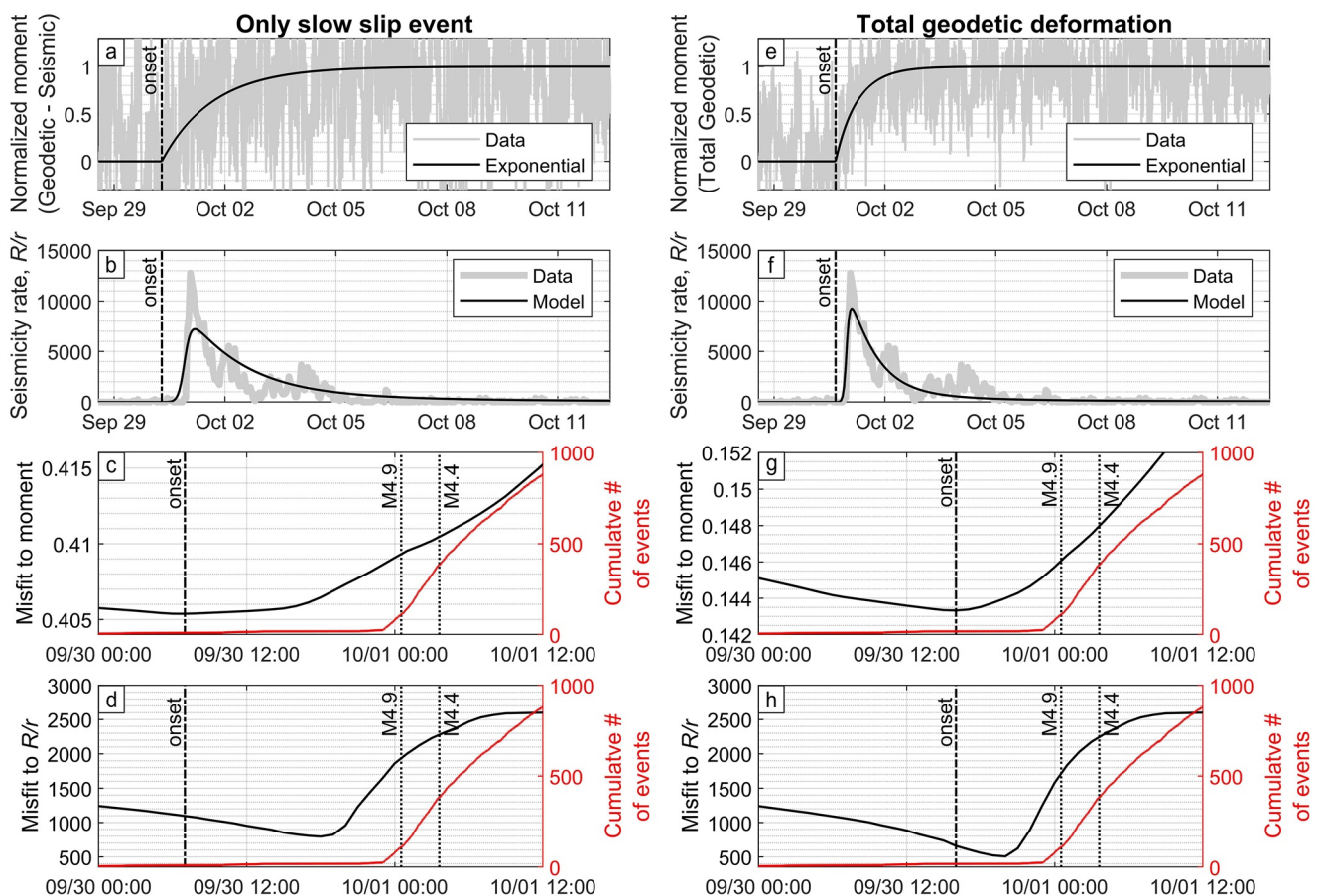


**Figure 11.** Exponential model fitting. Comparison of seismicity rate models driven by stress changes induced (a–d) by the slow slip event and (e–h) by the total geodetic deformation. For a homogeneous medium and stationary slip model, stress changes are proportional to the (a, e) moment release (unfiltered, normalized using the 5th and 95th percentiles), which can be approximated with an exponential function. (b, f) Best fit seismicity rate driven by the best fitted exponential stress changes. (c, g) Root-mean-squared-error (RMSE) misfit to the normalized moment and (d, h) and seismicity rate when varying the onset of the deformation. The seismicity rate used for modeling is derived from all detected events in our catalog, including those not relocated. The spatial distribution of seismicity is not considered.

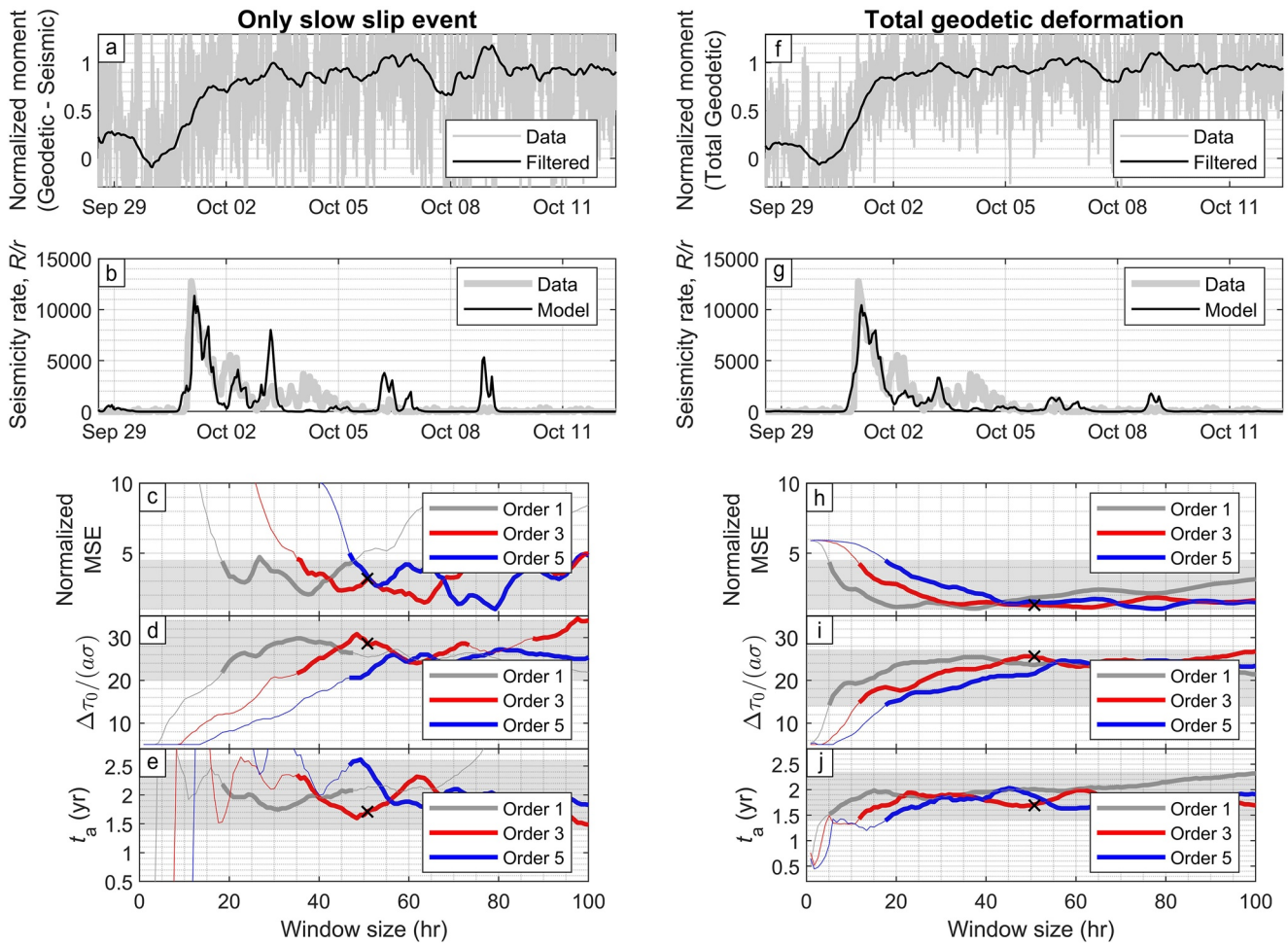


**Figure 12.** Savitzky-Golay filtered model fitting. Comparison of seismicity rate models driven by stress changes induced (a–e) by the slow slip event and (f–j) by the total geodetically resolved slip. For a homogeneous medium and stationary slip model, stress changes are proportional to the (a, f) moment release (unfiltered, normalized using the 5th and 95th percentiles), which can be filtered with a Savitzky-Golay filter based on moving 3rd order polynomial fit with 50 hr window. (b, g) Best fit seismicity rate. (c, h) Normalized mean squared error (MSE) from fitting the seismicity rate, (d, i) best fit  $\Delta\tau_0/a\sigma$  and (e, j) best fit  $t_a$  for the different window sizes and polynomial orders. The gray areas and thicker lines in (c–e, h–j) correspond to  $1\sigma$  confidence interval based on the chi-square criterion. The seismicity rate used for modeling is derived from all detected events in our catalog, including those not relocated. The spatial distribution of seismicity is not considered.

seismicity. The latter part of the swarm requires a secondary driving mechanism without significant geodetic deformation, such as pore-pressure diffusion (Section 5.7). We, therefore, choose to minimize RMSEs over only the first day of swarm activity. We summarize the RMSE and best fit parameters ( $\Delta\tau_0/a\sigma$  and  $t_a$ ) for various models in Table 2.

**Table 2**  
Root-Mean-Squared Error (RMSE) of Seismicity Rate Modeling and the Best Fit Parameters for the Different Models Tested in This Study

Driving stress	Denosing method	RMSE	$\tau_0/a\sigma$	$t_a$ (yr)
Slow slip event only	Heaviside step function	1,387	10.0	8.6
	Exponential function	1,097	24.6	2.6
	Savitzky-Golay filter (3rd order, 50 hr)	1,159	28.6	2.4
Total geodetically resolved slip	Heaviside step function	890	10.3	7.8
	Exponential function	661	23.0	2.0
	Savitzky-Golay filter (3rd order, 50 hr)	834	26.2	1.7
Total geodetically resolved slip (with threshold, Section 5.6)	Savitzky-Golay filter (3rd order, 50 hr)	702	74 ( $\tau_c/a\sigma = 18$ )	1.1

Our results suggest that the Heaviside step function (Figure S26 in Supporting Information S1) ignores the finite duration of the slow slip event, gives large misfits to moment and seismicity rates, and yields erroneous estimates of parameters. The models with exponential approximation (Figure 11) capture the main features and could be used to provide reliable estimates of  $\Delta\tau_0/a\sigma$  and  $t_a$ , though the peak seismicity rate is underestimated due to the smoothing effects. The exponential approximation can be useful when the details of the slip evolution are unavailable, as done in Lohman and McGuire (2007). However, further studies could assess the generalizability of this assumption as the model is an ad hoc analytical choice and is thus not based on any physical mechanism. Models using directly the Savitzky-Golay filtered cumulative moment release (Figure 12) best capture the detailed evolution of the seismicity rate. However, their misfit is larger than the exponential approximation due to noises that still persist even after the filter is applied. Furthermore, when comparing models driven by only slow slip event (left panels of Figures 11 and 12, Figure S26 in Supporting Information S1) with models driven by total geodetically resolved slip (right panels of Figures 11 and 12, Figure S26 in Supporting Information S1), we find that the latter performs better for all denoising methods tested. This means that even though the slow slip event plays a significant role in driving the swarm, the inter-earthquake static stress transfer is not negligible. We further quantify their relative contribution using point process statistics in Section 5.5.

Using denoising with the Savitzky-Golay filter, we further assess the effects of filtering parameters on the estimated parameters (Figures 12c–12e and 12h–12j). We vary the window size from 1 to 100 hr, use polynomial orders 1, 3, and 5, and find the window size of 50 hr and 3rd order polynomial preferable. While there are other options with smaller mean squared error (MSE), we find that they start to overfit the noises (Figures S27 and S28 in Supporting Information S1). If we were to choose such an overfitting model, it would not change the key conclusions of the study. Using chi-square criterion with  $1\sigma$  confidence interval ( $\Delta\chi^2 = \Delta\text{MSE} = 3.53$  for 3 degrees of freedom:  $\Delta\tau_0/a\sigma$ ,  $t_a$ , and filtering window size) to estimate the uncertainties of the parameters, we find  $\Delta\tau_0/a\sigma = 29_{-9}^{+5}$  and  $t_a = 1.7_{-0.3}^{+0.9}$  yr, when using a model driven by the slow slip event and  $\Delta\tau_0/a\sigma = 26_{-10}^{+11}$  and  $t_a = 1.7_{-0.3}^{+0.6}$  yr, when using a model driven by the total geodetically resolved slip. It is not unexpected that the estimated  $t_a$  is large compared to the swarm duration as the area still has an elevated seismicity rate several months after the swarm (Figure S29 in Supporting Information S1), though  $t_a$  may still be overestimated as the stress releases from events driven by pore-pressure diffusion are not accounted for in the model (Section 5.7). We discuss more how these values compare with other studies in Section 5.8.

Furthermore, given that the 5 min sampled position time series are considerably noisy (Figure 3c), the amount of time lag may be affected by the choice of filter used. We further quantify the uncertainty range of the time lag using Dieterich's model driven by an exponential stress change with different onset times. By fitting the moment release with the exponential function, we find that the best fit model has an onset with a time delay of 15 hr for those driven by only the slow slip event (Figures 11c) and 6 hr for those driven by total geodetically resolved slip (Figure 11g). Instead of selecting the best fit for the moment release, if we select the best fit based on the observed seismicity rate, the time delay of the onset shrinks considerably for both driving scenarios to 4 hr (Figures 11d) and 2 hr (Figure 11h), respectively. While misfits to the moment release and the seismicity rate increase only gradually as the time lag becomes longer, the misfits increase rapidly as the time lag becomes shorter than 2 hr. Therefore, the analysis supports that the time lag between the slow slip event and seismicity exists and cannot be an artifact of filtering. The best estimates yield a time lag between 2 and 15 hr, consistent with the onset derived from filtering the geodetic deformation with a Savitzky-Golay filter.

### 5.5. Seismicity as an Inhomogeneous Poisson Process

With Dieterich's model (Section 5.4), the earthquakes are assumed to be fully characterized by the Coulomb stress transfer. That is, seismicity follows an inhomogeneous Poisson process with varying seismicity rates  $R(t)/r$  governed by Equation 4. To test a posteriori if the observed seismicity follows an inhomogeneous Poisson process, we examine the distribution of times between consecutive seismic events  $\Delta t$ , hereafter referred to as the “interevent times.” In this section, we continue to treat the observed seismicity as a point process and do not consider spatial information. All detected events in our catalog, including those not relocated, are used.

For a homogeneous Poisson process with a constant seismicity rate  $\lambda$ , the interevent times  $\Delta t$  are expected to distribute exponentially, that is,  $\mathbb{P}(\Delta t) \sim \lambda e^{-\lambda\Delta t}$ . For an inhomogeneous Poisson process with varying seismicity rates  $\lambda(t)$ , interevent times would appear on average to be shorter than the exponential distribution due

to apparent clustering, as seen in the observed seismicity (Figure 13a). Any given inhomogeneous Poisson process can be converted to a homogeneous one if the evolving Poisson rates can be estimated. In our case, we can use the modeled seismicity rate  $R(t)/r$  from Section 5.4 that uses Savitzky-Golay filter as a denoising method (Figures 12b and 12d). The interevent times of the converted homogeneous Poisson process, referred to as the “modified interevent times,” can be calculated as follows:  $\Delta t_{\text{modified}} = \Delta t_{\text{observed}} \cdot R(t)/r$ , where  $R(t)/r$  is the modeled seismicity rate. Using the modeled seismicity rate from Dieterich's model driven by the slow slip event (Figure 12b), the  $\Delta t_{\text{modified}}$  follows better the exponential distribution (Figure 13b) than the  $\Delta t_{\text{observed}}$  (Figure 13a).  $\Delta t_{\text{modified}}$  follows even better the exponential distribution (Figure 13c) if the modeled seismicity rate from Dieterich's model driven by the total geodetic deformation (Figure 12d) is used. Regardless of the modeled seismicity rate used,  $\Delta t_{\text{modified}}$  is still shorter than expected by the exponential distribution suggesting that some level of clustered seismicity exists and is not captured by the inhomogeneity of seismicity rates.

The amount of clustering beyond those expected from the Poisson process can be quantified by fitting the interevent times distribution with a Gamma distribution,  $\mathbb{P}(\Delta t) \sim C \cdot \Delta t^{\gamma-1} \cdot e^{-\Delta t/\beta}$ , where  $C = (\beta^\gamma \Gamma(\gamma))^{-1}$  and  $\Gamma(x)$  is a Gamma function. If the interevent times  $\Delta t$  are normalized so that  $\overline{\Delta t} = 1$ , the fraction of clustered events is simply  $1 - \gamma$ , where  $\gamma = 1/\beta$  and  $\beta$  is the variance of the interevent times  $\sigma_{\Delta t}^2$  (Hainzl et al., 2006; Molchan, 2005). The Gamma distribution can explain clustering typically expected for aftershocks, but it fails to capture clustering due to the inhomogeneity of Poisson rates (Figure 13d). After removal of inhomogeneous Poisson rates using the modeled seismicity rate from Dieterich's model driven by the slow slip event (Figure 12b), we find that  $\Delta t_{\text{modified}}$  can be described by a Gamma distribution with  $\gamma = 0.6$ , meaning that the slow slip event can explain 60% of all

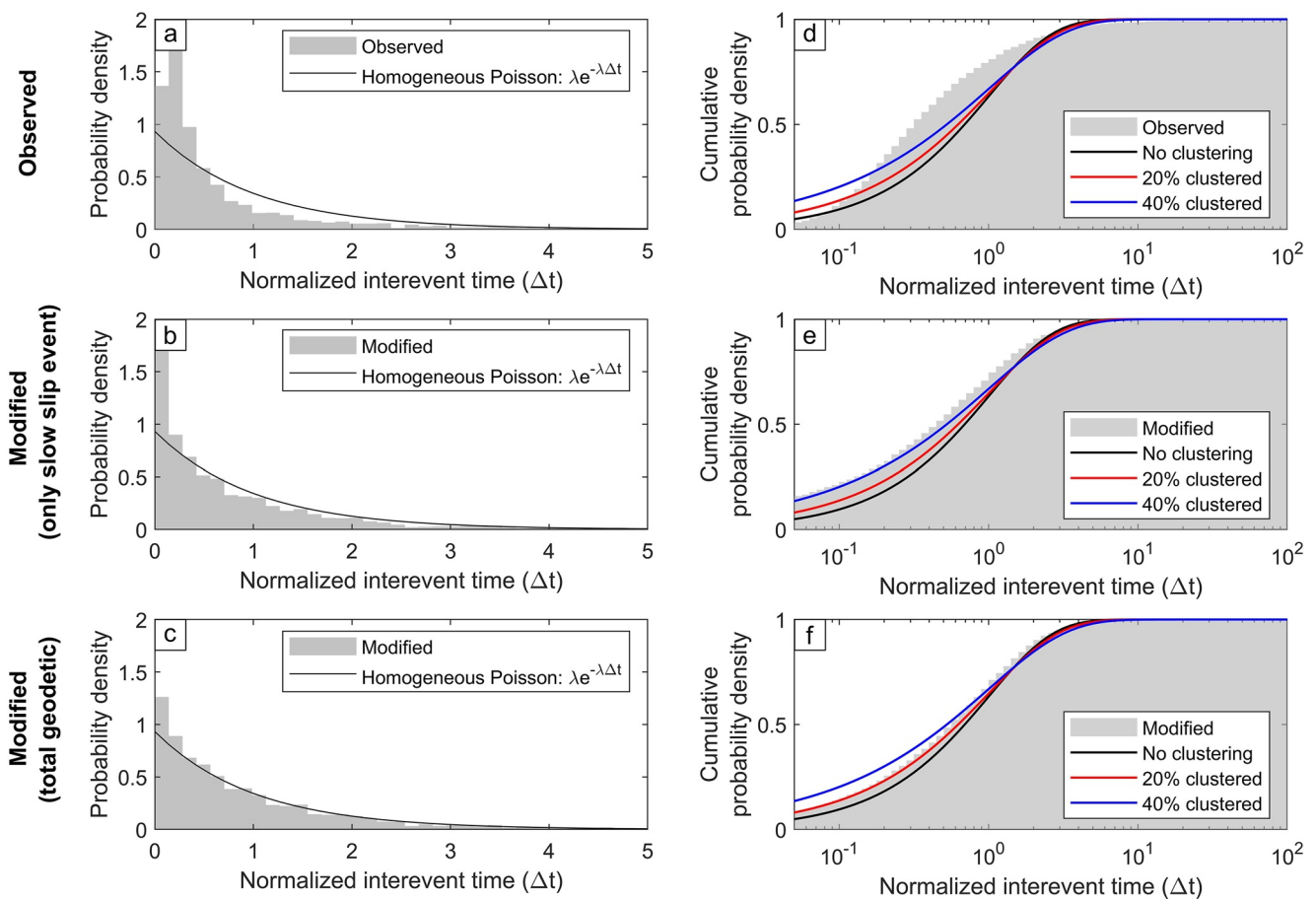


**Figure 13.** Statistics of times between seismic events. Comparison of the probability density of (a, d) the observed and the modified interevent times calculated by removing the inhomogeneity of seismicity rates using Dieterich's model driven by (b, e) the slow slip event and (c, f) total geodetic deformation which also includes the stress transfer from seismicity. The percentage of clustering is estimated using the Gamma distribution. This analysis does not consider spatial information and uses all detected events from this study, including those that are not relocated.

events, leaving 40% of unexplained clustered events (Figure 13e). On the other hand, if the rates are taken from Dieterich's model driven by the total geodetic deformation (Figure 12g),  $\Delta t_{\text{modified}}$  can be described by a Gamma distribution with  $\gamma = 0.8$ , meaning that the geodetic deformations (including both aseismic and seismic components) can explain 80% of all events, leaving only 20% unexplained clustered events (Figure 13f). The additional 20% of events explained by the total geodetic deformation but not by the slow slip event must then be explained by stress transfer from the seismic events, that is, inter-earthquake static stress triggering.

To further assess the reliability of the amount of clustering, we assume that Dieterich's model perfectly fits the data and examine  $\Delta t_{\text{modified}}$ . If the seismicity perfectly follows an inhomogeneous Poisson process,  $\Delta t_{\text{modified}}$  would be exactly exponentially distributed. Our analysis finds that this is not the case. Approximately 10% of  $\Delta t_{\text{modified}}$  with shortest durations are missing (Figure S30 in Supporting Information S1). Given that  $\Delta t_{\text{observed}} < 15$  seconds near the peak seismicity, this is likely due to under detection. Further analysis using a temporal variation of coefficient of variations (Kagan & Jackson, 1991) supports this interpretation (Text S3 and Figure S31 in Supporting Information S1). Accounting for this 10% of missed events, stress transfer from the slow slip event can explain at least 55% and potentially up to 64% of all events. The total geodetic deformation can explain at least 73% and potentially up to 82% of all events, meaning that  $\sim 10\%$ – $25\%$  can be explained with inter-earthquake static stress transfer. The remaining  $\sim 20\%$ – $30\%$  unexplained clustered events must then be accounted for by a secondary driver (Section 5.7).

### 5.6. Improving the Model With Stress Threshold

Even though Dieterich's model used in Section 5.4 can explain the overall evolution of the seismicity rate, it did not explain the sharp onset well. Previous studies have also encountered difficulty explaining the delayed onset and attributed it to the violation of the model assumptions that the system is well above the steady-state limit and is accelerating toward instability (Candela et al., 2019; Zhai et al., 2019). An introduction of thresholds in the form of critical stress (Bourne & Oates, 2017; Dempsey & Riffault, 2019; Dempsey & Suckale, 2017; Heimisson et al., 2021) or critical time (Zhai et al., 2019) can be implemented to improve the model. Introducing a critical time is a proxy for reducing a stress threshold that is valid if the stress changes are uniform in space. Here, we improve the model by adding a critical stress threshold  $\tau_c$  to Equation 4 following the formulation by Heimisson et al. (2021):

$$\frac{R(t)}{r} = 0 \text{ if } t < t_c$$

$$\frac{R(t)}{r} = \frac{e^{(\Delta\tau(t)-\Delta\tau_c)/a\sigma}}{1 + \frac{1}{t_a} \int_{t_c}^t e^{(\Delta\tau(x)-\Delta\tau_c)/a\sigma} dx} \text{ if } t \geq t_c \quad (5)$$

where  $t_c$  is the time when the stress threshold is first exceeded, that is,  $\Delta\tau(t = t_c) = \Delta\tau_c$ . With this modification, the longer time lag between the slow slip event and seismicity can be accounted for by increasing the stress threshold (Figure S32 in Supporting Information S1). By minimizing the RMSE over the swarm duration using a grid search, the best model yields a negligible threshold ( $< 1$  kPa). If we minimize the RMSE over only the first seismicity peak (up to the first day of the swarm), we find  $\Delta\tau_0/a\sigma = \Delta\tau(t = \infty)/a\sigma = 74$ ,  $\Delta\tau_c/a\sigma = 18$  and  $t_a = 1.1$  yr (Figure S33 in Supporting Information S1), and the model better captures the seismicity's sharp onset (Figure 14a). Using the average dCFS of 30 kPa (Figures 8a and 10c–10d) induced by the slow slip event at locations where we have earthquakes as  $\Delta\tau_0$ , we find  $a\sigma \sim 0.4$  kPa and hence  $\Delta\tau_c \sim 7.3$  kPa, a factor of 4 smaller than  $\Delta\tau_0$ .

To further assess the models, we generate two-dimensional synthetic catalogs of earthquakes along the fault plane F1. The driving dCFS is allowed to vary spatially along plane F1 (Figure 10a) and temporally according to the filtered aseismic moment release (Figure 12a). For each gridded cell, we calculate the expected seismicity rate using the best fit parameters from our models (Figure 14a), and seismicity is generated using the inverse transform sampling method (e.g., Zhuang & Touati, 2015). We refrain from using the total geodetically resolved slip in this analysis because our model does not capture the non-stationary nature of fault slip. We can better reproduce the spatial expansion of seismicity by enforcing the early part of fault slip to be a shallow slow slip event, as evident from comparing the spatial distribution of seismic and geodetic cumulative moment release (Section 4.2). Since Dieterich's model is highly nonlinear, the response to the time evolution of the integrated slip in space is not

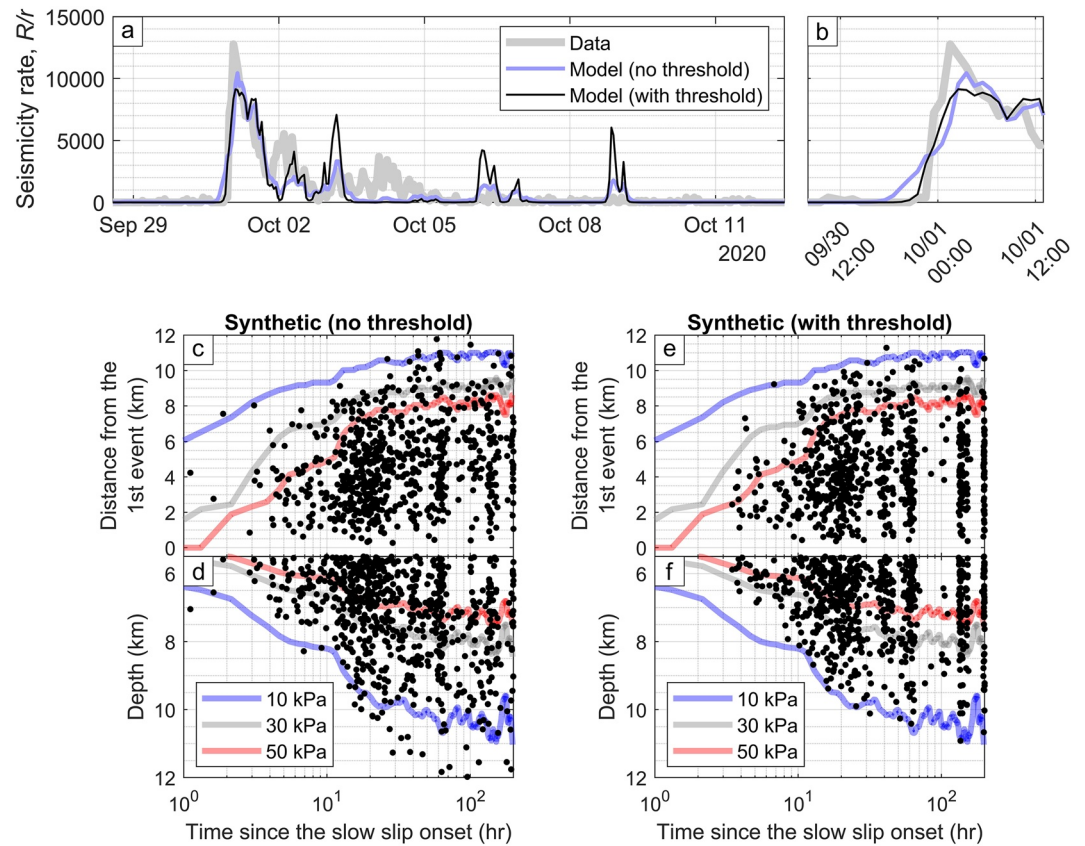


**Figure 14.** Effects of a stress threshold. (a) Modeled seismicity rate driven by total geodetically resolved deformation using stress-driven models based on Dieterich's nucleation (Dieterich, 1994) with and without stress threshold (Heimisson et al., 2021). (b) is a zoomed-in version of (a). Two-dimensional synthetic seismicity catalogs are generated using the best fit parameters for the (c–d) model without a threshold and (e–f) the model with a threshold. The spatial distribution of dCFS on fault plane F1 (Figure 10a) is plotted in panels (c–f) in the same way as Figures 10c and 10d. The onset of the slow slip event is picked to be  $\sim 8$  hr before the start of the swarm.

equal to the integrated response to the time evolution of slip at different spatial locations. Therefore, we cannot expect the number of events in the synthetic catalogs to match the observed catalogs. However, the synthetic catalogs can still capture first-order behaviors, such as the rapid expansion of seismicity and the time lag between the onset of the slow slip event and the swarm (Figures 14b–14e). We find the time lag from the model that includes a stress threshold more consistent with observations. Furthermore, we notice that the synthetic models cannot capture sharp boundaries that mark the extent of seismicity because of the smoothing imposed on the geodetic slip model used to calculate dCFS and the assumption that the seismicity productivity (the density of triggered earthquakes per unit of Coulomb stress increase) is homogeneous.

### 5.7. Pore-Pressure Diffusion as a Secondary Driver

Even though the swarm lasted for about 6 days, our geodetic observations find no significant surface deformation after the first day of the swarm. This, along with the poorer fit of the stress-driven model (Section 5.4 and Figure 12g) and the clustering behaviors (Section 5.5 and Figure S31 in Supporting Information S1), suggests that the latter phase of the swarm was driven by a secondary mechanism unrelated to the observed slow slip event. Abundant fluids in this hydrothermal area (Deane & Lynch, 2020) and the observation of a propagating back front marking an expansion of a zone of seismicity quiescence (Figures 5d and 15a), which is commonly observed in borehole fluid injection scenarios after the injection has terminated (e.g., Dahm et al., 2010; Parotidis et al., 2004, 2005; Shapiro & Dinske, 2009), leads us to propose pore-pressure diffusion as a possible secondary driver of the swarm.

With a point source fluid injection, we expect a leading seismicity front following the pore-pressure diffusion front with a square root of time expansion after the injection has started and a trailing propagating back front after the injection has terminated. A simple two-dimensional diffusive model (Paritidis et al., 2004) predicts that the back front  $r_{back}$  would expand as a function of time  $t$  according to the following equation:

$$r_{back}(t) = \sqrt{4 \cdot D \cdot t \cdot \left(\frac{t}{t_0} - 1\right) \cdot \ln\left(\frac{t}{t-t_0}\right)} \quad (8)$$

where  $D$  is the hydraulic diffusivity and  $t_0$  is the injection duration.

The back front is visible in our observations, but the leading front is not clear (Figure 15a). We attempt to fit the back front, assuming that the pore-pressure diffusion is mainly constrained along the 162°-striking main fault F1. A possible set of parameters that would fit well the back front include an injection location that is <1 km from the first relocated seismic event, a diffusivity of 4 m<sup>2</sup>/s, and an injection duration of 20 hr. The inferred leading seismicity front,  $r_{front}(t) = \sqrt{4Dt}$ , passes through the inferred origins (yellow and red stars in Figure 15) of seismicity expansion observed along the en-echelon fractures (structures E1 and E2 in blue boxes of Figure 5a with associated seismicity expansion annotated in Figure 5g). Given the proximity between the inferred injection location and the first seismic event, pore-pressure diffusion could be initiated by a seal that was broken because of the same stress changes that triggered the seismicity, similar to the scenario proposed for the Cahuilla swarm (Ross et al., 2020). Then, the en-echelon fractures were reactivated as the pore-pressure diffusion front arrived. However, given the obscured leading seismicity front, it is also plausible that fluids may have pre-existed in the main fault zone. The seals to the en-echelon fractures could then have broken arbitrarily in time, draining the fluids from the main fault zone and leading to the seismicity back front. The over-pressurized fault could also

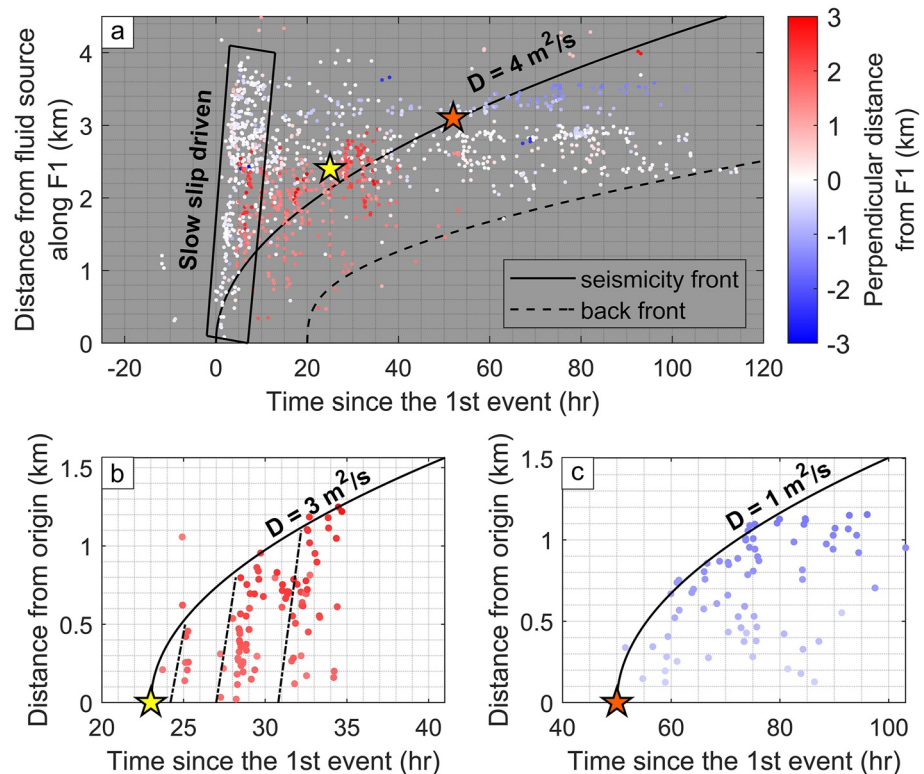


**Figure 15.** Pore-pressure diffusion as a secondary driver. (a) Expansion of seismicity along the 162°-striking main fault F1 (see geometry in Figure 5a) and along the en-echelon structures (b) E1 and (c) E2 (blue boxes in Figure 5a). The yellow and red stars are the inferred origin of expansion along the en-echelon structures. Seismic events here are from our relocated catalog, and they are all color-coded by the perpendicular distance from F1. For structure E1, the rapid expansion of seismicity at 25, 28, and 32 hr within the diffusive front are observed (dashed lines, panel (b)).

explain the poorer fit to Dieterich's model because normal stress changes may be larger relative to the effective normal stress, violating one of the model assumptions.

Upon reactivation of the en-echelon fractures, seismicity on these structures appears to expand as  $\sqrt{t}$  with inferred hydraulic diffusivities ranging from 1 to 3 m<sup>2</sup>/s (Figures 15b and 15c), slightly different from the 4 m<sup>2</sup>/s inferred for the main fault. The different diffusivities and hence the different permeabilities between the main fault and the en-echelon structures suggest that this fault zone is anisotropic, which could be caused by stress levels on the faults (e.g., Acosta et al., 2020), or geometry and maturity of the structures (e.g., Acosta & Violay, 2020; Caine et al., 1996; Jeanne et al., 2013).

The diffusivity values over the entire fault zone range from 1 to 4 m<sup>2</sup>/s, consistent with other swarms with a duration of a few days (Amezawa et al., 2021). This corresponds to permeabilities  $\sim 10^{-12}$ – $10^{-14}$  m<sup>2</sup> and porosity  $\sim 0.01$ – $0.2$  (Figure S34 in Supporting Information S1), similar to the values inferred from fluid-driven seismicity in other regions (e.g., Amezawa et al., 2021; Audin et al., 2002). These inferred permeabilities are quite large for intact rocks, but they are not unexpected for fractured metasedimentary rocks (e.g., Wong et al., 2013; Younker et al., 1982), particularly at low effective normal stresses (e.g., when pressurized fluids have permeated the fracture). In fractures subjected to low effective normal stress, fault slip can increase permeability by more than one order of magnitude (e.g., Guglielmi et al., 2015; Im et al., 2018; Lee & Cho, 2002; Yeo et al., 1998) due to low mechanical closure and low wear production rates, though this is not the case for fractures subjected to high effective normal stress (e.g., Acosta et al., 2020; Rutter & Mecklenburgh, 2018). The rapid migration of seismicity streaks (at times 25, 28, and 32 hr in Figure 15b) resembles features observed in other swarms, and that could be evidence of coupling between pore-pressure diffusion and the slow slip events (e.g., De Barros et al., 2020; Dublanche & De Barros, 2021) that were too insignificant to detect with current geodetic instrumentations. The velocities of these rapid migrations are between 0.6 and 0.8 km/hr, which is the same order-of-magnitude as the slow slip driven seismicity front observed along the main fault F1.

Because there is only minor inter-earthquake triggering (Sections 5.1 and 5.4), we can exclude the cascade model of earthquakes (Helmstetter & Sornette, 2002a) as a cause of the observed migration of the seismicity. Additionally, such a model would not produce a back front. Another possible interpretation of this zone of seismicity quiescence is stress shadow resulting from negative dCFS (Harris & Simpson, 1996, 1998, 2002). However, since most of the total dCFS was due to the slow slip event and large earthquakes that occurred within the first day of the swarm, this mechanism cannot explain how this zone continued to grow at a much later time. Therefore, we interpret that the slow slip event drove the early part of the sequence and fluid drove the latter, similar to the aftershocks of the 2010  $M_w$  7.2 El Mayor-Cucapah earthquake (Ross et al., 2017).

### 5.8. Estimating the Friction Parameter and Stress Conditions

Some fault properties, such as the frictional rate-and-state parameter  $a$  responsible for the nucleation process, cannot typically be measured in situ and require extrapolation from laboratory measurements (Marone, 1998). Other properties, such as the effective normal stress  $\sigma$ , in situ measurements are possible at shallow crustal depth but are very costly (e.g., Guglielmi et al., 2015). Studying the seismicity response to a known stress perturbation offers the possibility of estimating the product of the fault frictional rate-and-state parameter  $a$  and the in situ effective normal stress  $\sigma$ , providing constraints on fault properties. Some studies have estimated these parameters using seismicity responses to magmatic intrusions (Toda et al., 2002), solid Earth tidal or seasonal oscillations (Ader & Avouac, 2013; Bettinelli et al., 2008), reservoir loading (Rinaldi et al., 2020), slow slip events (Lohman & McGuire, 2007; Segall et al., 2006), or afterslip (Cattania et al., 2015). In this study, fitting seismicity rates with Dieterich's models with and without stress threshold gives us the parameter  $\Delta\tau_0/a\sigma$  (Table 2). Using the average dCFS induced by the slow slip event at locations where we have earthquakes ( $\sim 30$  kPa, see Figures 8a and 10c–10d) as  $\Delta\tau_0$ , we can calculate the corresponding product  $a\sigma$  (Table 3).

The estimates of parameter  $a\sigma$  from this study are between 0.4 and 1.2 kPa (Table 3), which is relatively small. For example, if we assume  $a \sim 0.001$ , a lower bound value typical of laboratory measurements (Marone, 1998), and use the overburden normal stress at 5 km of  $\sim 150$  MPa, we expect  $a\sigma \sim 150$  kPa. This suggests that either pore pressure is very large (99% of overburden stress), or the faults in the basement would have very small  $a$  ( $\sim 0.00001$ ), or a combination of both factors. Smaller  $a$  means that the earthquakes can nucleate with smaller driving stress.

**Table 3**

*Estimated Values of the Parameter  $a\sigma$  Using Independent Methods Based on Seismicity Responses to Different Types of Transient Driving Stresses*

Methods	$a\sigma$
Dieterich's model of the 2020 Westmorland swarm (Section 5.4)	1.2 kPa
Dieterich's model with stress threshold of the 2020 Westmorland swarm (Section 5.6)	0.4 kPa
Annual hydrological loads, using dCFS from Kreemer and Zaliapin (2018)	0.1 kPa
Annual hydrological loads, using dCFS from this study	<10 kPa
Semi-diurnal 12 hr tidal cycles, using dCFS from <i>Solid</i> software	>2.5 kPa

To further validate our estimates of  $a\sigma$ , we compare them with independent order-of-magnitude inferences using responses of seismicity to semi-diurnal (12 hr) tidal and annual hydrological stressing, which have been observed in natural faults (e.g., Ader & Avouac, 2013; Cochran et al., 2004; Tanaka et al., 2002; W. Wang et al., 2022; Wilcock, 2001) and in the laboratory (e.g., Bartlow et al., 2012; Beeler & Lockner, 2003; Chanard et al., 2019; Noël et al., 2019). We expect a larger response for smaller  $a\sigma$  (e.g., Ader et al., 2014; Beeler & Lockner, 2003; Heimisson & Avouac, 2020). To estimate the periodic variations of seismicity rate in the Westmorland area (latitude 32.98°–33.12°N, longitude 115.50°–115.65°W), we use the Quake Template Matching seismicity catalog (Ross, Trugman, et al., 2019). Since aftershocks are seismicity responses to the stress changes from the mainshocks, which are non-periodic, we first remove them by using the nearest-neighbor declustering approach (Zaliapin & Ben-Zion, 2013, 2020) based on a space-time-magnitude metric (Baiesi & Paczuski, 2004; Zaliapin et al., 2008) with a Gutenberg-Richter b-value estimated using maximum likelihood (Aki, 1965), as detailed in Text S4 and Figure S35 in Supporting Information S1. Then, we determine the amount of seismicity rate variation for a given periodicity using the Schuster p-value (Ader & Avouac, 2013; Schuster, 1897) and estimate the parameter  $a\sigma$  (Table 3) that best relates the periodic stressing to the observed seismicity rate variation (Ader et al., 2014), as detailed in Text S5 and Figures S36–S37 in Supporting Information S1. For annual period, seismicity rate variation is ~24%. Using the seasonal geodetic strains in Southern California of ~0.02 kPa (Kreemer & Zaliapin, 2018), we find  $a\sigma \sim 0.1$  kPa. These seasonal strains are relatively small when comparing to similar studies (e.g., Amos et al., 2014; C. W. Johnson et al., 2017), likely due to over smoothing. Alternatively, we can also use seasonal geodetic strains estimated from this study (IC7 in Figure S7 in Supporting Information S1). Without smoothing, displacements vary ~1 mm over 10 km of distances, resulting in an upper bound of geodetic strains of  $10^{-7}$ , which translates to  $a\sigma < 10$  kPa. For semi-diurnal (12 hr) period, seismicity shows insignificant periodicity with variations <26%. Using the semi-diurnal tidal strains of ~0.6 kPa estimated from surface displacements computed with *Solid* software (Milbert, 2018), as detailed in Text S6 and Figures S38–S39 in Supporting Information S1, we find  $a\sigma > 2.5$  kPa.

To conclude, the analysis of the 2020 Westmorland swarm provides local estimates of  $a\sigma \sim 0.4$ –1.2 kPa along with the patches of observed seismicity, while the hydrological and tidal analysis provides regional estimates of  $a\sigma \sim 2.5$ –10 kPa. While they are within one order-of-magnitude from one another, one way to interpret the differences is to attribute parts of the faults that ruptured during the 2020 Westmorland swarm to be weaker (smaller  $a\sigma$ ) than the surrounding areas, making them closer to failure and requiring less amount of driving stress to rupture. This weak zone might be related to the extent of the reservoir with pressurized fluid (and hence with lower effective normal stress  $\sigma$ ) bounded by impermeable rock layers.

Many studies utilizing Dieterich's model find a similar range of  $a\sigma$  between 1 and 40 kPa for various tectonic settings (Table 4), which is unexpectedly small. Recent dynamic simulations of two-dimensional finite faults found that the assumption of Dieterich's model that the product of slip velocity  $V$  and the state variable  $\theta$  is large compared to the critical slip distance  $D_{RS}$ , that is,  $V\theta/D_{RS} \gg 1$ , is often violated (e.g., Rubín & Ampuero, 2005), and as a result, the one-dimensional spring-slider system approximation leads to underestimation of  $a\sigma$  by 1–2 orders of magnitude (Ader et al., 2014; Kaneko & Lapusta, 2008). Using a more realistic estimate of  $a\sigma \sim 50$  kPa (~100 times our low bound of 0.4 kPa and ~5 times our upper bound of 10 kPa) and best fitted  $t_a \sim 1.7$  yr (Table 2), we estimate the background stressing rate  $\dot{\tau}_a = a\sigma/t_a \sim 30$  kPa/yr. This is consistent with the estimates using maximum total shear strain rate of ~1  $\mu$ strain/yr from GPS observations (Crowell et al., 2013), and an assumed shear modulus of 30 GPa resulted in a long-term stressing rate  $\dot{\tau} \sim 30$  kPa/yr.

**Table 4**  
*Estimated Parameter  $a\sigma$  for Different Studies of Various Tectonic Settings Based on the Seismicity Response to Transient Stresses*

Event	Estimated $a\sigma$
Aftershocks of the 1992 $M_w$ 7.3 Landers, California earthquake (Gross & Kisslinger, 1997)	20–40 kPa
Aftershocks of the 1989 $M_w$ 7.0 Loma Prieta, California earthquake (Gross & Bürgmann, 1998)	10 kPa
Aftershocks of the 2004 $M_w$ 6.0 Parkfield, California earthquake (Cattania et al., 2015)	3–8 kPa
Aftershocks of the 2011 $M_w$ 9.0 Tohoku, Japan earthquake (Cattania et al., 2015)	20–40 kPa
Izu volcanic island earthquake swarm, Japan (Toda et al., 2002)	30 kPa
Seasonal strains in the Himalayas (Bettinelli et al., 2008)	30 kPa
Reservoir-induced seismicity, Val d'Agri area, Italy (Rinaldi et al., 2020)	0.8 kPa
The 2020 Westmorland, California earthquake swarm (this study)	0.4–1.2 kPa
Seasonal strains and solid Earth tides, Westmorland, California (this study)	2.5–10 kPa

## 6. Discussion

### 6.1. Summarizing the 2020 Westmorland Swarm and the Mechanisms Involved

We conclude that the 2020 Westmorland swarm resulted from the interplay between a slow slip event, fluid diffusion, and seismic slip, as summarized in Figure 16 and Supporting Movie S5. The event began with an episode of shallow slow slip event (Section 4.2) occurring in the sedimentary cover, which induced a static stress change front that propagated as a logarithm of time (Section 5.3). Such stress change then drove the most critically stressed fault patches in the basement to rupture, forming a swarm of primarily non-interacting seismic events (Sections 5.4–5.6) that also expanded logarithmically with time (Section 5.3). A pore-pressure diffusion front could have started to expand as the square root of time after the stress change front broke the seal containing a pressurized fluid pocket. Upon reaching pre-existing en-echelon fractures orthogonal to the main fault, pressurized

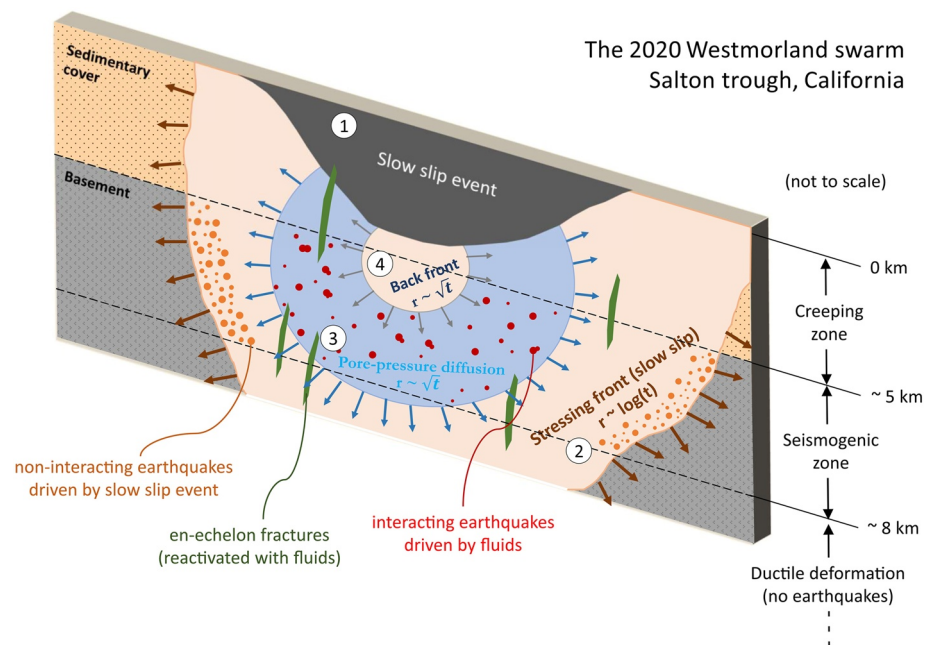


**Figure 16.** A schematic diagram summarizing the mechanics of the 2020 Westmorland swarm. The sequence started with (1) a spontaneous shallow slow slip event, which preceded the swarm by 2–15 hr. The slow slip event produced (2) Coulomb stress changes front propagating nonlinearly as a logarithm of time, triggering non-interacting earthquakes along the main fault. Behind this stressing front, there was (3) a pore-pressure diffusion front which drove seismicity on the main fault and reactivated seismicity on the en-echelon structures (green). Finally, (4) a propagating back front marked the termination of pore-pressure diffusion and the expansion of the zone of seismic quiescence.

fluid continued to migrate along these fractures causing seismicity on these structures that expanded diffusively as a square root of time with different apparent hydraulic diffusivities (Section 5.7). After the fluid pressure stabilized, seismicity terminated. As this zone of stability expanded as the square root of time, we observed a propagating back front marking the zone of seismicity quiescence (Section 5.7). The swarm terminated within  $\sim 5$  days, but the fits to seismicity using the stress-driven model with Dieterich's nucleation (Section 5.4) suggest that aftershocks should continue for  $\sim 1.7$  yr because of the time-dependent frictional response of faults. Using results from two independent analyses, static stress triggering (Section 5.1) and seismicity rate modeling with stress-driven models (Section 5.4–5.5), suggest that 45%–65% of seismicity was driven by the slow slip event, 10%–35% by inter-earthquake static stress transfer, and 10%–30% by fluid pressure changes.

We also find that lithology plays a significant role in determining the slip modes. The sedimentary cover (the top 5 km) primarily slips during aseismic slip events, while the shallow portion of the basement (between 5 and 8 km depth) primarily slips during earthquakes. Below this seismogenic zone (depth  $> 8$  km), the faults are probably mostly creeping from ductile deformation. For continental crust with strain rates of  $\sim 10^{-14}$  s, we expect the brittle-ductile transition (BDT) to occur at a temperature of  $\sim 400^{\circ}\text{C} \pm 100^{\circ}\text{C}$  (Violay et al., 2017). With a geothermal gradient of  $\sim 50^{\circ}\text{C}$ – $60^{\circ}\text{C}$  in the Westmorland area (Lachenbruch et al., 1985), the BDT is expected at 7–8 km depth, consistent with the observations. Furthermore, the observed deformation modes are consistent with the interseismic model based on geodetic data, which has a surface aseismic creep of 2.7 mm/yr and a locking depth of  $\sim 10$  km (Lindsey & Fialko, 2013). Earthquakes from the decades-long catalogs (e.g., Lin et al., 2007) are primarily within the 5–8 km depth range.

Finally, we try to estimate the contribution of swarms to long-term deformation. For example, if we compare the long-term slip rate of 17 mm/yr (Crowell et al., 2013) across the fault system with the average slip of  $\sim 20$  mm during the swarm, a return period of  $\sim 1$  yr would be needed if slip was only releasing as a result of repeated swarms similar to the Westmorland swarm of 2020. However, the seismicity catalog of Southern California clearly shows that the swarms do not return that frequently at Westmorland (Figure 1b). This disparity can be partially explained by the observation that the 2020 Westmorland swarm released less moment than a typical swarm in the area (e.g., Lohman & McGuire, 2007; Wei et al., 2015). Moreover, it may be possible that significant aseismic slip occurs in the period between swarms, either as a result of smaller episodic slow slip events or continuous creep.

## 6.2. Swarm as Aftershocks of the Slow Slip Event

The 2020 Westmorland swarm appears quite similar to afterslip-driven sequences of aftershocks (e.g., Perfettini & Avouac, 2007; Perfettini et al., 2018) but with the mainshock replaced by a slow slip event. The observed geodetic deformation associated with the 2020 Westmorland swarm shows rapid onset followed by deceleration (Figure 4), similar to the time evolution of afterslip (e.g., Ingleby & Wright, 2017; Marone et al., 1991; Perfettini & Avouac, 2004). The 2020 Westmorland swarm was also observed to expand logarithmically with time (Section 5.3), similar to the expansion of afterslip-driven aftershocks following large earthquakes (e.g., Frank et al., 2017; Kato & Obara, 2014; Peng & Zhao, 2009; Tang et al., 2014). For a sequence driven by a slow slip event that can be modeled with a logarithm function, the aftershocks are expected to expand as  $\log(t)$  regardless of whether there is a mainshock before the slow slip event or not (Perfettini et al., 2018). Once the slow slip event starts, the mechanisms that govern the evolution of swarms might be the same as those that drive aftershocks.

There are other swarms that have also been interpreted as aftershocks of slow slip events (e.g., Lohman & McGuire, 2007; Martínez-Garzón et al., 2021; Segall et al., 2006), but direct observational evidence in support of that interpretation is rare. This could be a common mechanism for swarms that would have gone unnoticed. Several studies provided evidence of aseismic deformation related to the swarm using radar interferometry, GPS, optical leveling data, or strainmeters (e.g., Kyriakopoulos et al., 2013; Lohman & McGuire, 2007; Wei et al., 2015; Wicks et al., 2011), but none had the time resolution needed to identify if the aseismic event preceded the swarms. Others have inferred aseismic forcing from seismicity data (Llenos & McGuire, 2011; Marsan et al., 2013). Detecting the preceding slow slip event, such as the one observed during the 2020 Westmorland swarm, requires access to high-rate GPS records in the near-field and the relatively sophisticated postprocessing of the geodetic time series. With limited observations thus far, it is uncertain whether the mechanics discussed in this study would generalize to other swarms in the Salton Trough or other tectonic settings worldwide.

## 7. Conclusions

The 2020 Westmorland swarm in the Salton Trough was exceptionally well-recorded by a dense array of seismometers, ground-based GPS/GNSS sites, and space-based radar interferometry, allowing us to describe the earthquake sequence with unprecedented details (Section 3). Our study provides evidence of a slow slip event starting between 2 and 15 hr before the swarm sequence (Section 4). We demonstrate their causal relationship using static stress triggering analysis (Sections 5.1–5.3) and Dieterich's stress-driven seismicity model based on rate-and-state friction (Sections 5.4–5.6). The model successfully explains the overall spatial and temporal evolution of seismicity, including the time lag between the slow slip event and seismicity, and provides constraints on the rate-and-state friction parameter  $a$  and pore pressure (Section 5.8). We have also identified pore-pressure diffusion as a secondary driver which sustains the swarm sequence, as supported by the existence of propagating back front and the square root of time expansion of reactivated seismicity along the orthogonal en-echelon structures (Section 5.7). Our analysis also allows us to quantify the relative contributions of the different mechanisms described: 45%–65% of seismicity was driven by the slow slip event, 10%–35% by inter-earthquake static stress transfer, and 10%–30% by fluids (Section 6.1). Our observations and modeling results are consistent with the interpretation of this swarm as aftershocks of a slow slip event sustained by fluid flow (Section 6.2).

## Data Availability Statement

Relocated seismicity catalogs, GPS data, InSAR data, geodetic slip model, and codes used to analyze them and generate figures are available through the CaltechDATA repository (<https://doi.org/10.22002/658vg-6xn94>; Sirorattanakul et al., 2022).

## References

- Acosta, M., Maye, R., & Violay, M. (2020). Hydraulic transport through calcite bearing faults with customized roughness: Effects of normal and shear loading. *Journal of Geophysical Research: Solid Earth*, 125(8), e2020JB019767. <https://doi.org/10.1029/2020JB019767>
- Acosta, M., & Violay, M. (2020). Mechanical and hydraulic transport properties of transverse-isotropic Gneiss deformed under deep reservoir stress and pressure conditions. *International Journal of Rock Mechanics and Mining Sciences*, 130, 104235. <https://doi.org/10.1016/j.ijrmm.2020.104235>
- Ader, T. J., & Avouac, J.-P. (2013). Detecting periodicities and declustering in earthquake catalogs using the Schuster spectrum, application to Himalayan seismicity. *Earth and Planetary Science Letters*, 377(378), 97–105. <https://doi.org/10.1016/j.epsl.2013.06.032>
- Ader, T. J., Lapusta, N., Avouac, J.-P., & Ampuero, J.-P. (2014). Response of rate-and-state seismogenic faults to harmonic shear-stress perturbations. *Geophysical Journal International*, 198(1), 385–413. <https://doi.org/10.1093/gji/ggu144>
- Aki, K. (1965). Maximum likelihood estimate of  $b$  in the formula  $\log N = a - bM$  and its confidence limits. *Bulletin of the Earthquake Research Institute, University of Tokyo*, 43, 237–239.
- Altamimi, Z., Rebischung, P., Métivier, L., & Collilieux, X. (2016). ITRF2014: A new release of the International Terrestrial Reference Frame modeling nonlinear station motions. *Journal of Geophysical Research: Solid Earth*, 121(8), 6109–6131. <https://doi.org/10.1002/2016JB013098>
- Amezawa, Y., Maeda, T., & Kosuga, M. (2021). Migration diffusivity as a controlling factor in the duration of earthquake swarms. *Earth Planets and Space*, 73(1), 148. <https://doi.org/10.1186/s40623-021-01480-7>
- Amos, C. B., Audet, P., Hammond, W. C., Bürgmann, R., Johanson, I. A., & Blewitt, G. (2014). Uplift and seismicity driven by groundwater depletion in central California. *Nature*, 509(7501), 483–486. <https://doi.org/10.1038/nature13275>
- Argus, D. F., Gordon, R. G., & DeMets, C. (2011). Geologically current motion of 56 plates relative to the no-net-rotation reference frame: NNR-MORVEL56. *Geochimistry, Geophysics, Geosystems*, 12(11). <https://doi.org/10.1029/2011GC003751>
- Audin, L., Avouac, J.-P., Flouzat, M., & Plantet, J.-L. (2002). Fluid-driven seismicity in a stable tectonic context: The Remiremont fault zone, Vosges, France. *Geophysical Research Letters*, 29(6), 131–134. <https://doi.org/10.1029/2001GL012988>
- Baiesi, M., & Paczuski, M. (2004). Scale-free networks of earthquakes and aftershocks. *Physical Review E*, 69(6), 066106. <https://doi.org/10.1103/PhysRevE.69.066106>
- Bartlow, N. M., Lockner, D. A., & Beeler, N. M. (2012). Laboratory triggering of stick-slip events by oscillatory loading in the presence of pore fluid with implications for physics of tectonic tremor. *Journal of Geophysical Research: Solid Earth*, 117(B11). <https://doi.org/10.1029/2012JB009452>
- Beeler, N. M., & Lockner, D. A. (2003). Why earthquakes correlate weakly with the solid Earth tides: Effects of periodic stress on the rate and probability of earthquake occurrence. *Journal of Geophysical Research*, 108(B8), 2391. <https://doi.org/10.1029/2001JB001518>
- Ben-Zion, Y., & Lyakhovskiy, V. (2006). Analysis of aftershocks in a lithospheric model with seismogenic zone governed by damage rheology. *Geophysical Journal International*, 165(1), 197–210. <https://doi.org/10.1111/j.1365-246X.2006.02878.x>
- Bettinelli, P., Avouac, J.-P., Flouzat, M., Bollinger, L., Ramillien, G., Rajure, S., & Sapkota, S. (2008). Seasonal variations of seismicity and geodetic strain in the Himalaya induced by surface hydrology. *Earth and Planetary Science Letters*, 266(3–4), 332–344. <https://doi.org/10.1016/j.epsl.2007.11.021>
- Bevis, M., & Brown, A. (2014). Trajectory models and reference frames for crustal motion geodesy. *Journal of Geodesy*, 88(3), 283–311. <https://doi.org/10.1007/s00190-013-0685-5>
- Bhattacharya, P., & Viesca, R. C. (2019). Fluid-induced aseismic fault slip outpaces pore-fluid migration. *Science*, 364(6439), 464–468. <https://doi.org/10.1126/science.aaw7354>
- Bird, P. (2003). An updated digital model of plate boundaries. *Geochemistry, Geophysics, Geosystems*, 4(3). <https://doi.org/10.1029/2001GC000252>

## Acknowledgments

The authors thank Sebastian Hainzl, Kathryn Materna, the associate editor, editor Satoshi Ide, and one anonymous reviewer for insightful and detailed comments, which greatly helped improve the quality of the manuscript. Generic Mapping Tool version 6 (Wessel et al., 2019) and Matlab version 2020a were used to analyze data and prepare figures. This work greatly benefited from the seismic waveform and seismic catalogs accessible from the Southern California Seismic Network data repository (<https://scedc.caltech.edu>), processed 5 min and daily sampled GPS data from Nevada Geodetic Laboratory (<http://geodesy.unr.edu/>; Blewitt et al., 2018), and C-band Synthetic Aperture Radar (SAR) images acquired by the Sentinel-1 satellite (available through Copernicus Open Access Hub: <https://scihub.copernicus.eu/>), along with seismic phase association software PhaseLink (<https://github.com/interseismic/PhaseLink>); Ross, Yue, et al., (2019), hypocenter inversion software HypoSVI (<https://github.com/Ulvetanna/HypoSVI>; Smith et al., 2021), earthquake relocations software GrowClust (<https://github.com/dtrugman/GrowClust>; Trugman & Shearer, 2017), independent component analysis software vblCA (Gualandi & Pintori, 2020), Schuster spectrum software ([http://www.tectonics.caltech.edu/resources/schuster\\_spectrum/](http://www.tectonics.caltech.edu/resources/schuster_spectrum/); Ader & Avouac, 2013), and solid Earth tides calculation software solid (Milbert, 2018). The authors thank Adriano Gualandi for providing codes

for GPS processing and Coulomb stress calculations. This research is partly supported by the National Science Foundation (NSF) Grants EAR-1821853 and EAR-2034167 and the University of Southern California / Southern California Earthquake Center Grant SC0N-00003725. M.A. is funded by the Swiss National Science Foundation (SNF) Grant PZELP2\_195127. Any use of trade, firm, or product names is for descriptive purposes only and does not imply endorsement by the U.S. Government.

- Blewitt, G., Hammond, W., & Kreemer, C. (2018). Harnessing the GPS data explosion for interdisciplinary science. *Eos*, 99. <https://doi.org/10.1029/2018EO104623>
- Bourne, S. J., & Oates, S. J. (2017). Extreme threshold failures within a heterogeneous elastic thin sheet and the spatial-temporal development of induced seismicity within the Groningen gas field. *Journal of Geophysical Research: Solid Earth*, 122(12), 10299–10310. <https://doi.org/10.1002/2017JB014356>
- Brothers, D. S., Driscoll, N. W., Kent, G. M., Harding, A. J., Babcock, J. M., & Baskin, R. L. (2009). Tectonic evolution of the Salton Sea inferred from seismic reflection data. *Nature Geoscience*, 2(8), 581–584. <https://doi.org/10.1038/ngeo590>
- Caine, J. S., Evans, J. P., & Forster, C. B. (1996). Fault zone architecture and permeability structure. *Geology*, 24(11), 1025. [https://doi.org/10.1130/0091-7613\(1996\)024<1025:FZAAAPS>2.3.CO;2](https://doi.org/10.1130/0091-7613(1996)024<1025:FZAAAPS>2.3.CO;2)
- Candela, T., Osinga, S., Ampuero, J., Wassing, B., Pluymaekers, M., Fokker, P. A., et al. (2019). Depletion-induced seismicity at the Groningen gas field: Coulomb rate-and-state models including differential compaction effect. *Journal of Geophysical Research: Solid Earth*, 124(7), 7081–7104. <https://doi.org/10.1029/2018JB016670>
- Cappa, F., Rutqvist, J., & Yamamoto, K. (2009). Modeling crustal deformation and rupture processes related to upwelling of deep CO<sub>2</sub>-rich fluids during the 1965–1967 Matsushiro earthquake swarm in Japan. *Journal of Geophysical Research*, 114(B10), B10304. <https://doi.org/10.1029/2009JB006398>
- Cattania, C., Hainzl, S., Wang, L., Enescu, B., & Roth, F. (2015). Aftershock triggering by postseismic stresses: A study based on Coulomb rate-and-state models. *Journal of Geophysical Research: Solid Earth*, 120(4), 2388–2407. <https://doi.org/10.1002/2014JB011500>
- Chan, K., Lee, T.-W., & Sejnowski, T. J. (2003). Variational Bayesian Learning of ICA with missing data. *Neural Computation*, 15(8), 1991–2011. <https://doi.org/10.1162/08997660360675116>
- Chanard, K., Nicolas, A., Hatano, T., Petrelis, F., Latour, S., Vinciguerra, S., & Schubnel, A. (2019). Sensitivity of acoustic emission triggering to small pore pressure cycling perturbations during brittle creep. *Geophysical Research Letters*, 46(13), 7414–7423. <https://doi.org/10.1029/2019GL082093>
- Chen, C. W., & Zebker, H. A. (2001). Two-dimensional phase unwrapping with use of statistical models for cost functions in nonlinear optimization. *Journal of the Optical Society of America A*, 18(2), 338. <https://doi.org/10.1364/JOSA.A.18.000338>
- Chen, X., & Shearer, P. M. (2011). Comprehensive analysis of earthquake source spectra and swarms in the Salton Trough, California. *Journal of Geophysical Research*, 116(B9), B09309. <https://doi.org/10.1029/2011JB008263>
- Chen, X., Shearer, P. M., & Abercrombie, R. E. (2012). Spatial migration of earthquakes within seismic clusters in Southern California: Evidence for fluid diffusion. *Journal of Geophysical Research: Solid Earth*, 117(B4). <https://doi.org/10.1029/2011JB008973>
- Chiaraluce, L., Valoroso, L., Piccinini, D., Di Stefano, R., & De Gori, P. (2011). The anatomy of the 2009 L'Aquila normal fault system (central Italy) imaged by high-resolution foreshock and aftershock locations. *Journal of Geophysical Research*, 116(B12), B12311. <https://doi.org/10.1029/2011JB008352>
- Choudrey, R. A., & Roberts, S. J. (2003). Variational mixture of Bayesian Independent Component Analyzers. *Neural Computation*, 15(1), 213–252. <https://doi.org/10.1162/089976603321043766>
- Cochran, E. S., Vidale, J. E., & Tanaka, S. (2004). Earth tides can trigger shallow thrust fault earthquakes. *Science*, 306(5699), 1164–1166. <https://doi.org/10.1126/science.1103961>
- Crowell, B. W., Bock, Y., Sandwell, D. T., & Fialko, Y. (2013). Geodetic investigation into the deformation of the Salton Trough. *Journal of Geophysical Research: Solid Earth*, 118(9), 5030–5039. <https://doi.org/10.1002/jgrb.50347>
- Dahm, T., Hainzl, S., & Fischer, T. (2010). Bidirectional and unidirectional fracture growth during hydrofracturing: Role of driving stress gradients. *Journal of Geophysical Research*, 115(B12), B12322. <https://doi.org/10.1029/2009JB006817>
- Deane, R. T., & Lynch, D. K. (2020). *A moving mud spring threatening critical infrastructure, Imperial County, California*. In *Geo-Congress 2020* (pp. 717–727). American Society of Civil Engineers. <https://doi.org/10.1061/9780784482797.070>
- De Barros, L., Cappa, F., Deschamps, A., & Dublanche, P. (2020). Imbricated aseismic slip and fluid diffusion drive a seismic swarm in the Corinth Gulf, Greece. *Geophysical Research Letters*, 47(9). <https://doi.org/10.1029/2020GL087142>
- Dempsey, D., & Riffault, J. (2019). Response of induced seismicity to injection rate reduction: Models of delay, decay, quiescence, recovery, and Oklahoma. *Water Resources Research*, 55(1), 656–681. <https://doi.org/10.1029/2018WR023587>
- Dempsey, D., & Suckale, J. (2017). Physics-based forecasting of induced seismicity at Groningen gas field, the Netherlands. *Geophysical Research Letters*, 44(15), 7773–7782. <https://doi.org/10.1002/2017GL073878>
- Dieterich, J. H. (1979). Modeling of rock friction: 1. Experimental results and constitutive equations. *Journal of Geophysical Research*, 84(B5), 2161. <https://doi.org/10.1029/JB084iB05p02161>
- Dieterich, J. H. (1981). *Constitutive properties of faults with simulated gouge*. In N. L. Carter, M. Friedman, J. M. Logan, & D. W. Stearns (Eds.), *Geophysical Monograph Series* (pp. 103–120). American Geophysical Union. <https://doi.org/10.1029/GM024p0103>
- Dieterich, J. H. (1994). A constitutive law for rate of earthquake production and its application to earthquake clustering. *Journal of Geophysical Research: Solid Earth*, 99(B2), 2601–2618. <https://doi.org/10.1029/93JB02581>
- Dieterich, J. H., Cayol, V., & Okubo, P. (2000). The use of earthquake rate changes as a stress meter at Kilauea volcano. *Nature*, 408(6811), 457–460. <https://doi.org/10.1038/35044054>
- Dublanche, P. (2019). Fluid driven shear cracks on a strengthening rate-and-state frictional fault. *Journal of the Mechanics and Physics of Solids*, 132, 103672. <https://doi.org/10.1016/j.jmps.2019.07.015>
- Dublanche, P., & De Barros, L. (2021). Dual seismic migration velocities in seismic swarms. *Geophysical Research Letters*, 48(1). <https://doi.org/10.1029/2020GL090025>
- Efron, B., & Stein, C. (1981). The Jackknife estimate of variance. *Annals of Statistics*, 9(3), 586–596. <https://doi.org/10.1214/aos/1176345462>
- Ellsworth, W. L., & Beroza, G. C. (1995). Seismic evidence for an earthquake nucleation phase. *Science*, 268, 6. <https://doi.org/10.1126/science.268.5212.851>
- European Space Agency. (2014). Sentinel-1 SAR user guide. Retrieved from <https://sentinels.copernicus.eu/web/sentinel/user-guides/sentinel-1-sar>
- Farr, T. G., Rosen, P. A., Caro, E., Crippen, R., Duren, R., Hensley, S., et al. (2007). The Shuttle Radar Topography Mission. *Reviews of Geophysics*, 45(2), RG2004. <https://doi.org/10.1029/2005RG000183>
- Fischer, T., Horálek, J., Hrubcová, P., Vavryčuk, V., Bräuer, K., & Kämpf, H. (2014). Intra-continental earthquake swarms in West-Bohemia and Vogtland: A review. *Tectonophysics*, 611, 1–27. <https://doi.org/10.1016/j.tecto.2013.11.001>
- Franceschetti, G., & Lanari, R. (1999). *Synthetic aperture radar processing* (1st ed.). CRC Press.
- Frank, W. B., Poli, P., & Perfettini, H. (2017). Mapping the rheology of the Central Chile subduction zone with aftershocks. *Geophysical Research Letters*, 44(11), 5374–5382. <https://doi.org/10.1002/2016GL072288>

- Fuis, G. S., Mooney, W. D., Healy, J. H., McMechan, G. A., & Lutter, W. J. (1984). A seismic refraction survey of the Imperial Valley Region, California. *Journal of Geophysical Research: Solid Earth*, 89(B2), 1165–1189. <https://doi.org/10.1029/JB089iB02p01165>
- Google Earth V 7.3. (2020). Salton Sea. Retrieved from <http://www.earth.google.com>
- Got, J.-L., Monteiller, V., Guilbert, J., Marsan, D., Cansi, Y., Maillard, C., & Sautoire, J.-P. (2011). Strain localization and fluid migration from earthquake relocation and seismicity analysis in the western Vosges (France). *Geophysical Journal International*, 185(1), 365–384. <https://doi.org/10.1111/j.1365-246X.2011.04944.x>
- Gross, S., & Bürgmann, R. (1998). Rate and state of background stress estimated from the aftershocks of the 1989 Loma Prieta, California, earthquake. *Journal of Geophysical Research: Solid Earth*, 103(B3), 4915–4927. <https://doi.org/10.1029/97JB03010>
- Gross, S., & Kisslinger, C. (1997). Estimating tectonic stress rate and state with Landers aftershocks. *Journal of Geophysical Research: Solid Earth*, 102(B4), 7603–7612. <https://doi.org/10.1029/96JB03741>
- Gualandi, A., Liu, Z., & Rollins, C. (2020). Post-large earthquake seismic activities mediated by aseismic deformation processes. *Earth and Planetary Science Letters*, 530, 115870. <https://doi.org/10.1016/j.epsl.2019.115870>
- Gualandi, A., Nichele, C., Serpelloni, E., Chiaraluce, L., Anderlini, L., Latorre, D., et al. (2017). Aseismic deformation associated with an earthquake swarm in the northern Apennines (Italy). *Geophysical Research Letters*, 44(15), 7706–7714. <https://doi.org/10.1002/2017GL073687>
- Gualandi, A., & Pintori, F. (2020). vbICA code (version 1). Retrieved from <https://doi.org/10.17632/n92vwbg8zt.1>
- Gualandi, A., Serpelloni, E., & Belardinelli, M. E. (2016). Blind source separation problem in GPS time series. *Journal of Geodesy*, 90(4), 323–341. <https://doi.org/10.1007/s00190-015-0875-4>
- Guglielmi, Y., Cappa, F., Avouac, J.-P., Henry, P., & Elsworth, D. (2015). Seismicity triggered by fluid injection-induced aseismic slip. *Science*, 348(6240), 1224–1226. <https://doi.org/10.1126/science.aab0476>
- Hainzl, S. (2016). Rate-dependent incompleteness of earthquake catalogs. *Seismological Research Letters*, 87(2A), 337–344. <https://doi.org/10.1785/0220150211>
- Hainzl, S., Fischer, T., Čermáková, H., Bachura, M., & Vlček, J. (2016). Aftershocks triggered by fluid intrusion: Evidence for the after-shock sequence occurred 2014 in West Bohemia/Vogtland. *Journal of Geophysical Research: Solid Earth*, 121(4), 2575–2590. <https://doi.org/10.1002/2015JB012582>
- Hainzl, S., Fischer, T., & Dahm, T. (2012). Seismicity-based estimation of the driving fluid pressure in the case of swarm activity in Western Bohemia: Seismicity-based fluid pressure estimation. *Geophysical Journal International*, 191(1), 271–281. <https://doi.org/10.1111/j.1365-246X.2012.05610.x>
- Hainzl, S., Scherbaum, F., & Beauval, C. (2006). Estimating background activity based on interevent-time distribution. *Bulletin of the Seismological Society of America*, 96(1), 313–320. <https://doi.org/10.1785/0120050053>
- Hansen, P. C. (1992). Analysis of discrete ill-posed problems by means of the *L*-curve. *SIAM Review*, 34(4), 561–580. <https://doi.org/10.1137/1034115>
- Harris, R. A., & Simpson, R. W. (1996). In the shadow of 1857—the effect of the Great Ft. Tejon earthquake on subsequent earthquakes in Southern California. *Geophysical Research Letters*, 23(3), 229–232. <https://doi.org/10.1029/96GL00015>
- Harris, R. A., & Simpson, R. W. (1998). Suppression of large earthquakes by stress shadows: A comparison of Coulomb and rate-and-state failure. *Journal of Geophysical Research: Solid Earth*, 103(B10), 24439–24451. <https://doi.org/10.1029/98JB00793>
- Harris, R. A., & Simpson, R. W. (2002). The 1999  $M_w$  7.1 Hector Mine, California, earthquake: A test of the stress shadow hypothesis? *Bulletin of the Seismological Society of America*, 92(4), 1497–1512. <https://doi.org/10.1785/0120000913>
- Hatch, R. L., Abercrombie, R. E., Ruhl, C. J., & Smith, K. D. (2020). Evidence of aseismic and fluid-driven processes in a small complex seismic swarm near Virginia City, Nevada. *Geophysical Research Letters*, 47(4), e2019GL085477. <https://doi.org/10.1029/2019GL085477>
- Hauksson, E. (2015). Average stress drops of Southern California earthquakes in the context of crustal geophysics: Implications for fault zone healing. *Pure and Applied Geophysics*, 172(5), 1359–1370. <https://doi.org/10.1007/s00024-014-0934-4>
- Hauksson, E., Meier, M., Ross, Z. E., & Jones, L. M. (2017). Evolution of seismicity near the southernmost terminus of the San Andreas Fault: Implications of recent earthquake clusters for earthquake risk in Southern California. *Geophysical Research Letters*, 44(3), 1293–1301. <https://doi.org/10.1002/2016GL072026>
- Hauksson, E., Yang, W., & Shearer, P. M. (2012). Waveform relocated earthquake catalog for Southern California (1981 to June 2011). *Bulletin of the Seismological Society of America*, 102(5), 2239–2244. <https://doi.org/10.1785/0120120010>
- Heimisson, E. R. (2019). Constitutive law for earthquake production based on rate-and-state friction: Theory and application of interacting sources. *Journal of Geophysical Research: Solid Earth*, 124(2), 1802–1821. <https://doi.org/10.1029/2018JB016823>
- Heimisson, E. R., & Avouac, J.-P. (2020). Analytical prediction of seismicity rate due to tides and other oscillating stresses. *Geophysical Research Letters*, 47(23). <https://doi.org/10.1029/2020GL090827>
- Heimisson, E. R., & Segall, P. (2018). Constitutive law for earthquake production based on rate-and-state friction: Dieterich 1994 revisited. *Journal of Geophysical Research: Solid Earth*, 123(5), 4141–4156. <https://doi.org/10.1029/2018JB015656>
- Heimisson, E. R., Smith, J. D., Avouac, J.-P., & Bourne, S. J. (2021). Coulomb threshold rate-and-state model for fault reactivation: Application to induced seismicity at Groningen. *Geophysical Journal International*, 228(3), 2061–2072. <https://doi.org/10.1093/gji/ggab467>
- Heinicke, J., Fischer, T., Gaupp, R., Götze, J., Koch, U., Konietzky, H., & Stanek, K.-P. (2009). Hydrothermal alteration as a trigger mechanism for earthquake swarms: The Vogtland/NW Bohemia region as a case study. *Geophysical Journal International*, 178(1), 1–13. <https://doi.org/10.1111/j.1365-246X.2009.04138.x>
- Helmstetter, A., & Sornette, D. (2002a). Diffusion of epicenters of earthquake aftershocks, Omori's law, and generalized continuous-time random walk models. *Physical Review E*, 66(6), 061104. <https://doi.org/10.1103/PhysRevE.66.061104>
- Helmstetter, A., & Sornette, D. (2002b). Subcritical and supercritical regimes in epidemic models of earthquake aftershocks. *Journal of Geophysical Research: Solid Earth*, 107(B10), ESE 10-1–ESE 10-21. <https://doi.org/10.1029/2001JB001580>
- Holtkamp, S. G., & Brudzinski, M. R. (2011). Earthquake swarms in circum-Pacific subduction zones. *Earth and Planetary Science Letters*, 305(1–2), 215–225. <https://doi.org/10.1016/j.epsl.2011.03.004>
- Hooper, A., Segall, P., & Zebker, H. (2007). Persistent scatterer interferometric synthetic aperture radar for crustal deformation analysis, with application to Volcán Alcedo, Galápagos. *Journal of Geophysical Research*, 112(B7), B07407. <https://doi.org/10.1029/2006JB004763>
- Hoskins, M. C., Meltzer, A., Font, Y., Agurto-Detzel, H., Vaca, S., Rolandone, F., et al. (2021). Triggered crustal earthquake swarm across subduction segment boundary after the 2016 Pedernales, Ecuador megathrust earthquake. *Earth and Planetary Science Letters*, 553, 116620. <https://doi.org/10.1016/j.epsl.2020.116620>
- Hubbert, M. K., & Rubey, W. W. (1959). Role of fluid pressure in mechanics of overthrust faulting. *Bulletin of the Geological Society of America*, 70, 115–166.
- Huiskamp, G. (1991). Difference formulas for the surface Laplacian on a triangulated surface. *Journal of Computational Physics*, 95(2), 477–496. [https://doi.org/10.1016/0021-9991\(91\)90286-T](https://doi.org/10.1016/0021-9991(91)90286-T)

- Hutton, K., Woessner, J., & Hauksson, E. (2010). Earthquake monitoring in Southern California for 77 yr (1932–2008). *Bulletin of the Seismological Society of America*, *100*(2), 423–446. <https://doi.org/10.1785/0120090130>
- Im, K., & Avouac, J.-P. (2021). On the role of thermal stress and fluid pressure in triggering seismic and aseismic faulting at the Brawley Geothermal Field, California. *Geothermics*, *97*, 102238. <https://doi.org/10.1016/j.geothermics.2021.102238>
- Im, K., Elsworth, D., & Fang, Y. (2018). The influence of preslip sealing on the permeability evolution of fractures and faults. *Geophysical Research Letters*, *45*(1), 166–175. <https://doi.org/10.1002/2017GL076216>
- Ingleby, T., & Wright, T. J. (2017). Omori-like decay of postseismic velocities following continental earthquakes. *Geophysical Research Letters*, *44*(7), 3119–3130. <https://doi.org/10.1002/2017GL072865>
- Jeanne, P., Guglielmi, Y., & Cappa, F. (2013). Hydromechanical heterogeneities of a mature fault zone: Impacts on fluid flow. *Groundwater*, *51*(6), 880–892. <https://doi.org/10.1111/gwat.12017>
- Jiang, Y., Samsonov, S. V., & González, P. J. (2022). Aseismic fault slip during a shallow normal-faulting seismic swarm constrained using a physically informed geodetic inversion method. *Journal of Geophysical Research: Solid Earth*, *127*(7). <https://doi.org/10.1029/2021JB022621>
- Johnson, C. E., & Hill, D. P. (1982). Seismicity of the Imperial Valley. In *The Imperial Valley, California, earthquake of 15 October 1979* (Vol. 1254, pp. 15–24). U.S. Geological Survey Professional Paper.
- Johnson, C. W., Fu, Y., & Bürgmann, R. (2017). Seasonal water storage, stress modulation, and California seismicity. *Science*, *356*(6343), 1161–1164. <https://doi.org/10.1126/science.aak9547>
- Jónsson, S., Zebker, H., Segall, P., & Amelung, F. (2002). Fault slip distribution of the 1999  $M_w$  7.1 Hector Mine, California, earthquake, estimated from satellite radar and GPS measurements. *Bulletin of the Seismological Society of America*, *92*(4), 1377–1389. <https://doi.org/10.1785/0120000922>
- Kagan, Y. Y., & Jackson, D. D. (1991). Long-term earthquake clustering. *Geophysical Journal International*, *104*(1), 117–134. <https://doi.org/10.1111/j.1365-246X.1991.tb02498.x>
- Kanamori, H., & Anderson, D. L. (1975). Theoretical basis of some empirical relations in Seismology. *Bulletin of the Seismological Society of America*, *65*(5), 1073–1095.
- Kaneko, Y., & Lapusta, N. (2008). Variability of earthquake nucleation in continuum models of rate-and-state faults and implications for after-shock rates. *Journal of Geophysical Research*, *113*(B12), B12312. <https://doi.org/10.1029/2007JB005154>
- Kato, A., & Obara, K. (2014). Step-like migration of early aftershocks following the 2007  $M_w$  6.7 Noto-Hanto earthquake, Japan: Kato and Obara: Step-like migration of early aftershocks. *Geophysical Research Letters*, *41*(11), 3864–3869. <https://doi.org/10.1002/2014GL060427>
- King, G. C. P., Stein, R. S., & Lin, J. (1994). Static stress changes and the triggering of earthquakes. *Bulletin of the Seismological Society of America*, *84*(3), 935–953.
- Kositsky, A. P., & Avouac, J.-P. (2010). Inverting geodetic time series with a principal component analysis-based inversion method. *Journal of Geophysical Research*, *115*(B3), B03401. <https://doi.org/10.1029/2009JB006535>
- Kreemer, C., & Zaliapin, I. (2018). Spatiotemporal correlation between seasonal variations in seismicity and horizontal dilatational strain in California. *Geophysical Research Letters*, *45*(18), 9559–9568. <https://doi.org/10.1029/2018GL079536>
- Kyriakopoulos, C., Chini, M., Bignami, C., Stramondo, S., Ganas, A., Kolligri, M., & Moshou, A. (2013). Monthly migration of a tectonic seismic swarm detected by DInSAR: Southwest Peloponnese, Greece. *Geophysical Journal International*, *194*(3), 1302–1309. <https://doi.org/10.1093/gji/ggt196>
- Lachenbruch, A. H., Sass, J. H., & Galanis, S. P. (1985). Heat flow in southernmost California and the origin of the Salton Trough. *Journal of Geophysical Research*, *90*(B8), 6709. <https://doi.org/10.1029/JB090iB08p06709>
- Laroche, S., Gualandi, A., Chanard, K., & Avouac, J.-P. (2018). Identification and extraction of seasonal geodetic signals due to surface load variations. *Journal of Geophysical Research: Solid Earth*, *123*(12). <https://doi.org/10.1029/2018JB016607>
- Laroche, S., Lapusta, N., Ampuero, J., & Cappa, F. (2021). Constraining fault friction and stability with fluid-injection field experiments. *Geophysical Research Letters*, *48*(10). <https://doi.org/10.1029/2020GL091188>
- Lee, H. S., & Cho, T. F. (2002). Hydraulic characteristics of rough fractures in linear flow under normal and shear load. *Rock Mechanics and Rock Engineering*, *35*(4), 299–318. <https://doi.org/10.1007/s00603-002-0028-y>
- Lévesque, J.-J., Rivera, L., & Wittlinger, G. (1993). On the use of the checker-board test to assess the resolution of tomographic inversions. *Geophysical Journal International*, *115*(1), 313–318. <https://doi.org/10.1111/j.1365-246X.1993.tb05605.x>
- Lin, G., Shearer, P. M., & Hauksson, E. (2007). Applying a three-dimensional velocity model, waveform cross-correlation, and cluster analysis to locate Southern California seismicity from 1981 to 2005. *Journal of Geophysical Research*, *112*(B12), B12309. <https://doi.org/10.1029/2007JB004986>
- Lindsey, E. O., & Fialko, Y. (2013). Geodetic slip rates in the southern San Andreas Fault system: Effects of elastic heterogeneity and fault geometry. *Journal of Geophysical Research: Solid Earth*, *118*(2), 689–697. <https://doi.org/10.1029/2012JB009358>
- Llenos, A. L., & McGuire, J. J. (2011). Detecting aseismic strain transients from seismicity data. *Journal of Geophysical Research*, *116*(B6), B06305. <https://doi.org/10.1029/2010JB007537>
- Lohman, R. B., & McGuire, J. J. (2007). Earthquake swarms driven by aseismic creep in the Salton Trough, California. *Journal of Geophysical Research: Solid Earth*, *112*(B4). <https://doi.org/10.1029/2006JB004596>
- Mallat, S. G. (1989). A theory for multiresolution signal decomposition: The wavelet representation. *IEEE Transactions on Pattern Analysis and Machine Intelligence*, *11*(7), 674–693. <https://doi.org/10.1109/34.192463>
- Marone, C. (1998). Laboratory-derived friction laws and their application to seismic faulting. *Annual Review of Earth and Planetary Sciences*, *26*(1), 643–696. <https://doi.org/10.1146/annurev.earth.26.1.643>
- Marone, C., Scholtz, C. H., & Bilham, R. (1991). On the mechanics of earthquake afterslip. *Journal of Geophysical Research*, *96*(B5), 8441. <https://doi.org/10.1029/91JB00275>
- Marsan, D., Prono, E., & Helmstetter, A. (2013). Monitoring aseismic forcing in fault zones using earthquake time series. *Bulletin of the Seismological Society of America*, *103*(1), 169–179. <https://doi.org/10.1785/0120110304>
- Martínez-Garzón, P., Durand, V., Bentz, S., Kwiatek, G., Dresen, G., Turkmen, T., et al. (2021). Near-fault monitoring reveals combined seismic and slow activation of a fault branch within the Istanbul-Marmara seismic gap in northwest Turkey. *Seismological Research Letters*, *92*(6), 3743–3756. <https://doi.org/10.1785/0220210047>
- Materna, K., Barbour, A., Jiang, J., & Eneva, M. (2022). Detection of aseismic slip and poroelastic reservoir deformation at the North Brawley Geothermal Field from 2009 to 2019. *Journal of Geophysical Research: Solid Earth*, *127*(5). <https://doi.org/10.1029/2021JB023335>
- Michel, S., Gualandi, A., & Avouac, J.-P. (2019). Interseismic coupling and slow slip events on the Cascadia megathrust. *Pure and Applied Geophysics*, *176*(9), 3867–3891. <https://doi.org/10.1007/s00024-018-1991-x>
- Milbert, D. (2018). Solid (version 2018 to 7 june). Retrieved from <https://geodesyworld.github.io/SOFTS/solid.htm>

- Mogi, K. (1963). Some discussions on aftershocks, foreshocks and earthquake swarms—The fracture of a semi-infinite body caused by an inner stress origin and its relation to the earthquake phenomena (3rd paper). *Bulletin of the Earthquake Research Institute, University of Tokyo*, 41(3), 615–658.
- Molchan, G. (2005). Intervent time distribution in seismicity: A theoretical approach. *Pure and Applied Geophysics*, 162(6–7), 1135–1150. <https://doi.org/10.1007/s00024-004-2664-5>
- Nishikawa, T., & Ide, S. (2017). Detection of earthquake swarms at subduction zones globally: Insights into tectonic controls on swarm activity: Detection of Earthquake Swarms. *Journal of Geophysical Research: Solid Earth*, 122(7), 5325–5343. <https://doi.org/10.1002/2017JB014188>
- Nishikawa, T., & Ide, S. (2018). Recurring slow slip events and earthquake nucleation in the source region of the M 7 Ibaraki-Oki earthquakes revealed by earthquake swarm and foreshock activity. *Journal of Geophysical Research: Solid Earth*, 123(9), 7950–7968. <https://doi.org/10.1029/2018JB015642>
- Noda, H., Lapusta, N., & Kanamori, H. (2013). Comparison of average stress drop measures for ruptures with heterogeneous stress change and implications for earthquake physics. *Geophysical Journal International*, 193(3), 1691–1712. <https://doi.org/10.1093/gji/ggt074>
- Noël, C., Passetlègue, F. X., Giorgetti, C., & Violay, M. (2019). Fault reactivation during fluid pressure oscillations: Transition from stable to unstable slip. *Journal of Geophysical Research: Solid Earth*, 124(11), 10940–10953. <https://doi.org/10.1029/2019JB018517>
- Nur, A., & Booker, J. R. (1972). Aftershocks caused by pore fluid flow? *Science*, 175(4024), 885–887. <https://doi.org/10.1126/science.175.4024.885>
- Ogata, Y. (1988). Statistical models for earthquake occurrences and residual analysis for point processes. *Journal of the American Statistical Association*, 83(401), 9–27. <https://doi.org/10.1080/01621459.1988.10478560>
- Ogata, Y. (1992). Detection of precursory relative quiescence before great earthquakes through a statistical model. *Journal of Geophysical Research*, 97(B13), 19845. <https://doi.org/10.1029/92JB00708>
- Okada, Y. (1985). Surface deformation due to shear and tensile faults in a half-space. *Bulletin of the Seismological Society of America*, 75(4), 1135–1154. <https://doi.org/10.1785/BSSA0750041135>
- Okada, Y. (1992). Internal deformation due to shear and tensile faults in a half-space. *Bulletin of the Seismological Society of America*, 82(2), 1018–1040. <https://doi.org/10.1785/BSSA0820021018>
- Omori, F. (1894). On the aftershocks of earthquakes. *Journal of the College of Science, Imperial University of Tokyo*, 7, 111–200.
- Parotidis, M., Shapiro, S. A., & Rothert, E. (2004). Back front of seismicity induced after termination of borehole fluid injection. *Geophysical Research Letters*, 31(2). <https://doi.org/10.1029/2003GL018987>
- Parotidis, M., Shapiro, S. A., & Rothert, E. (2005). Evidence for triggering of the Vogtland swarms 2000 by pore pressure diffusion. *Journal of Geophysical Research*, 110(B5), B05S10. <https://doi.org/10.1029/2004JB003267>
- Passarelli, L., Hainzl, S., Cesca, S., Maccaferri, F., Mucciarelli, M., Roessler, D., et al. (2015). Aseismic transient driving the swarm-like seismic sequence in the Pollino range, Southern Italy. *Geophysical Journal International*, 201(3), 1553–1567. <https://doi.org/10.1093/gji/ggv111>
- Peng, Z., & Zhao, P. (2009). Migration of early aftershocks following the 2004 Parkfield earthquake. *Nature Geoscience*, 2(12), 877–881. <https://doi.org/10.1038/ngeo697>
- Perfettini, H., & Avouac, J.-P. (2004). Postseismic relaxation driven by brittle creep: A possible mechanism to reconcile geodetic measurements and the decay rate of aftershocks, application to the Chi-Chi earthquake, Taiwan. *Journal of Geophysical Research: Solid Earth*, 109(B2). <https://doi.org/10.1029/2003JB002488>
- Perfettini, H., & Avouac, J.-P. (2007). Modeling afterslip and aftershocks following the 1992 Landers earthquake. *Journal of Geophysical Research*, 112(B7), B07409. <https://doi.org/10.1029/2006JB004399>
- Perfettini, H., Frank, W. B., Marsan, D., & Bouchon, M. (2018). A model of aftershock migration driven by afterslip. *Geophysical Research Letters*, 45(5), 2283–2293. <https://doi.org/10.1002/2017GL076287>
- Rinaldi, A. P., Improta, L., Hainzl, S., Catali, F., Urpi, L., & Wiemer, S. (2020). Combined approach of poroelastic and earthquake nucleation applied to the reservoir-induced seismic activity in the Val d'Agri area, Italy. *Journal of Rock Mechanics and Geotechnical Engineering*, 12(4), 802–810. <https://doi.org/10.1016/j.jrmge.2020.04.003>
- Robinson, P. T., & Elders, W. A. (1976). Quaternary volcanism in the Salton Sea geothermal field, Imperial Valley, California. *The Geological Society of America Bulletin*, 87, 347–360. [https://doi.org/10.1130/0016-7606\(1976\)87<347:qvits>2.0.co;2](https://doi.org/10.1130/0016-7606(1976)87<347:qvits>2.0.co;2)
- Rockwell, T., Scharer, K., & Dawson, T. (2016). Earthquake geology and paleoseismology of major strands of the San Andreas fault system. In *Applied geology in California* (Vol. 26). Association of Environmental and Engineering Geology Special Publication.
- Roland, E., & McGuire, J. J. (2009). Earthquake swarms on transform faults. *Geophysical Journal International*, 178(3), 1677–1690. <https://doi.org/10.1111/j.1365-246X.2009.04214.x>
- Roman, D. C., & Cashman, K. V. (2006). The origin of volcano-tectonic earthquake swarms. *Geology*, 34(6), 457. <https://doi.org/10.1130/G22269.1>
- Ross, Z. E., & Cochran, E. S. (2021). Evidence for latent crustal fluid injection transients in Southern California from long-duration earthquake swarms. *Geophysical Research Letters*, 48(12). <https://doi.org/10.1029/2021GL092465>
- Ross, Z. E., Cochran, E. S., Trugman, D. T., & Smith, J. D. (2020). 3D fault architecture controls the dynamism of earthquake swarms. *Science*, 368(6497), 1357–1361. <https://doi.org/10.1126/science.abb0779>
- Ross, Z. E., Rollins, C., Cochran, E. S., Hauksson, E., Avouac, J.-P., & Ben-Zion, Y. (2017). Aftershocks driven by afterslip and fluid pressure sweeping through a fault-fracture mesh. *Geophysical Research Letters*, 44(16), 8260–8267. <https://doi.org/10.1002/2017GL074634>
- Ross, Z. E., Trugman, D. T., Hauksson, E., & Shearer, P. M. (2019). Searching for hidden earthquakes in Southern California. *Science*, 364(6442), 767–771. <https://doi.org/10.1126/science.aaw6888>
- Ross, Z. E., Yue, Y., Meier, M., Hauksson, E., & Heaton, T. H. (2019). PhaseLink: A deep learning approach to seismic phase association. *Journal of Geophysical Research: Solid Earth*, 124(1), 856–869. <https://doi.org/10.1029/2018JB016674>
- Rubin, A. M., & Ampuero, J.-P. (2005). Earthquake nucleation on (aging) rate and state faults. *Journal of Geophysical Research: Solid Earth*, 110(B11). <https://doi.org/10.1029/2005JB003686>
- Ruina, A. (1983). Slip instability and state variable friction laws. *Journal of Geophysical Research: Solid Earth*, 88(B12), 10359–10370. <https://doi.org/10.1029/JB088iB12p10359>
- Rutter, E. H., & Mecklenburgh, J. (2018). Influence of normal and shear stress on the hydraulic transmissivity of thin cracks in a tight Quartz Sandstone, a Granite, and a Shale. *Journal of Geophysical Research: Solid Earth*, 123(2), 1262–1285. <https://doi.org/10.1002/2017JB014858>
- Sáez, A., Lecampion, B., Bhattacharya, P., & Viesca, R. C. (2022). Three-dimensional fluid-driven stable frictional ruptures. *Journal of the Mechanics and Physics of Solids*, 160, 104754. <https://doi.org/10.1016/j.jmps.2021.104754>
- Savitzky, A., & Golay, M. J. E. (1964). Smoothing and differentiation of data by simplified least squares procedures. *Analytical Chemistry*, 36(8), 1627–1639. <https://doi.org/10.1021/ac60214a047>
- SCEDC. (2013). Southern California Earthquake Data Center. Retrieved from <https://scedc.caltech.edu/>

- Schuster, A. (1897). On lunar and solar periodicities of earthquakes. *Proceedings of the Royal Society of London*, 61, 455–465. <https://doi.org/10.1038/056321a0>
- Segall, P., Desmarais, E. K., Shelly, D., Miklius, A., & Cervelli, P. (2006). Earthquakes triggered by silent slip events on Kilauea volcano, Hawaii. *Nature*, 442(7098), 71–74. <https://doi.org/10.1038/nature04938>
- Serpelloni, E., Pintori, F., Gualandi, A., Scocimarro, E., Cavaliere, A., Anderlini, L., et al. (2018). Hydrologically induced Karst deformation: Insights from GPS measurements in the Adria-Eurasia plate boundary zone. *Journal of Geophysical Research: Solid Earth*, 123(5), 4413–4430. <https://doi.org/10.1002/2017JB015252>
- Shapiro, S. A., & Dinske, C. (2009). Fluid-induced seismicity: Pressure diffusion and hydraulic fracturing. *Geophysical Prospecting*, 57(2), 301–310. <https://doi.org/10.1111/j.1365-2478.2008.00770.x>
- Shapiro, S. A., Huenges, E., & Borm, G. (1997). Estimating the crust permeability from fluid-injection-induced seismic emission at the KTB site. *Geophysical Journal International*, 131(2), F15–F18. <https://doi.org/10.1111/j.1365-246X.1997.tb01215.x>
- Shapiro, S. A., Rother, E., Rath, V., & Rindschwentner, J. (2002). Characterization of fluid transport properties of reservoirs using induced microseismicity. *Geophysics*, 67(1), 212–220. <https://doi.org/10.1190/1.1451597>
- Sharma, V., Wadhawan, M., Rana, N., Sreejith, K. M., Agrawal, R., Kamra, C., et al. (2020). A long-duration non-volcanic earthquake sequence in the stable continental region of India: The Palghar swarm. *Tectonophysics*, 779, 228376. <https://doi.org/10.1016/j.tecto.2020.228376>
- Shaw, J. H., Plesch, A., Tape, C., Suess, M. P., Jordan, T. H., Ely, G., et al. (2015). Unified structural representation of the Southern California crust and upper mantle. *Earth and Planetary Science Letters*, 415, 1–15. <https://doi.org/10.1016/j.epsl.2015.01.016>
- Shelly, D. R., Ellsworth, W. L., & Hill, D. P. (2016). Fluid-faulting evolution in high definition: Connecting fault structure and frequency-magnitude variations during the 2014 Long Valley Caldera, California, earthquake swarm: Fluid-Faulting Evolution in Long Valley. *Journal of Geophysical Research: Solid Earth*, 121(3), 1776–1795. <https://doi.org/10.1002/2015JB012719>
- Shelly, D. R., & Hardebeck, J. L. (2019). Illuminating faulting complexity of the 2017 Yellowstone Maple Creek earthquake swarm. *Geophysical Research Letters*, 46(5), 2544–2552. <https://doi.org/10.1029/2018GL081607>
- Shelly, D. R., Moran, S. C., & Thelen, W. A. (2013). Evidence for fluid-triggered slip in the 2009 Mount Rainier, Washington earthquake swarm. *Geophysical Research Letters*, 40(8), 1506–1512. <https://doi.org/10.1002/grl.50354>
- Shirzaei, M. (2013). A wavelet-based multitemporal DInSAR algorithm for monitoring ground surface motion. *IEEE Geoscience and Remote Sensing Letters*, 10(3), 456–460. <https://doi.org/10.1109/LGRS.2012.2208935>
- Shirzaei, M., & Bürgmann, R. (2012). Topography correlated atmospheric delay correction in radar interferometry using wavelet transforms. *Geophysical Research Letters*, 39(1). <https://doi.org/10.1029/2011gl049971>
- Shirzaei, M., & Walter, T. R. (2011). Estimating the effect of satellite orbital error using wavelet-based robust regression applied to InSAR deformation data. *IEEE Transactions on Geoscience and Remote Sensing*, 49(11), 4600–4605. <https://doi.org/10.1109/TGRS.2011.2143419>
- Sirorattanakul, K., Ross, Z. E., Khoshmanesh, M., Cochran, E. S., Acosta, M., & Avouac, J.-P. (2022). Supporting data and codes for the 2020 Westmorland, California earthquake swarm as aftershocks of a slow slip event sustained by fluid flow [CaltechDATA]. <https://doi.org/10.22002/658vg-6xn94>
- Smith, J. D., Ross, Z. E., Azizzadenesheli, K., & Muir, J. B. (2021). HypoSVI: Hypocentre inversion with Stein variational inference and physics informed neural networks. *Geophysical Journal International*, 228(1), 698–710. <https://doi.org/10.1093/gji/ggab309>
- Tanaka, S., Ohtake, M., & Sato, H. (2002). Evidence for tidal triggering of earthquakes as revealed from statistical analysis of global data. *Journal of Geophysical Research: Solid Earth*, 107(B10), ESE 1–1–ESE 1–11. <https://doi.org/10.1029/2001JB001577>
- Tang, C.-C., Lin, C.-H., & Peng, Z. (2014). Spatial-temporal evolution of early aftershocks following the 2010 ML 6.4 Jiashian earthquake in southern Taiwan. *Geophysical Journal International*, 199(3), 1772–1783. <https://doi.org/10.1093/gji/ggu361>
- Thomas, M. Y., Avouac, J.-P., Champenois, J., Lee, J.-C., & Kuo, L.-C. (2014). Spatiotemporal evolution of seismic and aseismic slip on the Longitudinal Valley Fault, Taiwan. *Journal of Geophysical Research: Solid Earth*, 119(6), 5114–5139. <https://doi.org/10.1002/2013JB010603>
- Toda, S., Stein, R. S., & Sagiya, T. (2002). Evidence from the AD 2000 Izu islands earthquake swarm that stressing rate governs seismicity. *Nature*, 419(6902), 58–61. <https://doi.org/10.1038/nature00997>
- Trugman, D. T., & Shearer, P. M. (2017). GrowClust: A hierarchical clustering algorithm for relative earthquake relocation, with application to the Spanish Springs and Sheldon, Nevada, earthquake sequences. *Seismological Research Letters*, 88(2A), 379–391. <https://doi.org/10.1785/0220160188>
- U.S. Geological Survey and California Geological Survey. Quaternary fault and fold database for the United States. Retrieved from <https://www.usgs.gov/programs/earthquake-hazards/faults>
- Utsu, T. (1961). A statistical study on the occurrence of aftershocks. *Geophysical Magazine*, 30, 521–605.
- Vidale, J. E., & Shearer, P. M. (2006). A survey of 71 earthquake bursts across Southern California: Exploring the role of pore fluid pressure fluctuations and aseismic slip as drivers. *Journal of Geophysical Research*, 111(B5). <https://doi.org/10.1029/2005JB004034>
- Violay, M., Heap, M. J., Acosta, M., & Madonna, C. (2017). Porosity evolution at the brittle-ductile transition in the continental crust: Implications for deep hydro-geothermal circulation. *Scientific Reports*, 7(1), 7705. <https://doi.org/10.1038/s41598-017-08108-5>
- Wang, C., Ding, X., Li, Q., & Jiang, M. (2014). Equation-based InSAR data quadtree downsampling for earthquake slip distribution inversion. *IEEE Geoscience and Remote Sensing Letters*, 11(12), 2060–2064. <https://doi.org/10.1109/LGRS.2014.2318775>
- Wang, W., Shearer, P. M., Vidale, J. E., Xu, X., Trugman, D. T., & Fialko, Y. (2022). Tidal modulation of seismicity at the Coso geothermal field. *Earth and Planetary Science Letters*, 579, 117335. <https://doi.org/10.1016/j.epsl.2021.117335>
- Wei, S., Avouac, J.-P., Hudnut, K. W., Donnellan, A., Parker, J. W., Graves, R. W., et al. (2015). The 2012 Brawley swarm triggered by injection-induced aseismic slip. *Earth and Planetary Science Letters*, 422, 115–125. <https://doi.org/10.1016/j.epsl.2015.03.054>
- Werner, C., Wegmüller, U., Strozzi, T., & Wiesmann, A. (2000). Gamma SAR and interferometric processing software. In *Proceedings of the ERS-ENVISAT Symposium*.
- Wessel, P., Luis, J. F., Uieda, L., Scharroo, R., Wobbe, F., Smith, W. H. F., & Tian, D. (2019). The generic mapping tools version 6. *Geochemistry, Geophysics, Geosystems*, 20(11), 5556–5564. <https://doi.org/10.1029/2019GC008515>
- Wessel, P., & Smith, W. H. F. (1996). A global, self-consistent, hierarchical, high-resolution shoreline database. *Journal of Geophysical Research: Solid Earth*, 101(B4), 8741–8743. <https://doi.org/10.1029/96JB00104>
- Wicks, C., Thelen, W., Weaver, C., Gomberg, J., Rohay, A., & Bodin, P. (2011). InSAR observations of aseismic slip associated with an earthquake swarm in the Columbia River flood basalts. *Journal of Geophysical Research*, 116(B12), B12304. <https://doi.org/10.1029/2011JB008433>
- Wilcock, W. S. D. (2001). Tidal triggering of microearthquakes on the Juan de Fuca Ridge. *Geophysical Research Letters*, 28(20), 3999–4002. <https://doi.org/10.1029/2001GL013370>
- Wong, L. N. Y., Li, D., & Liu, G. (2013). Experimental studies on permeability of intact and singly jointed meta-sedimentary rocks under confining pressure. *Rock Mechanics and Rock Engineering*, 46(1), 107–121. <https://doi.org/10.1007/s00603-012-0251-0>

- Yang, W., & Hauksson, E. (2013). The tectonic crustal stress field and style of faulting along the Pacific North America Plate boundary in Southern California. *Geophysical Journal International*, *194*(1), 100–117. <https://doi.org/10.1093/gji/ggt113>
- Yeo, I. W., Freitas, M. H. D., & Zimmerman, R. W. (1998). Effect of shear displacement on the aperture and permeability of a rock fracture. *International Journal of Rock Mechanics and Mining Sciences*, *35*(8), 1051–1070. [https://doi.org/10.1016/S0148-9062\(98\)00165-X](https://doi.org/10.1016/S0148-9062(98)00165-X)
- Younker, L. W., Kasameyer, P. W., & Tewhey, J. D. (1982). Geological, geophysical, and thermal characteristics of the Salton Sea Geothermal Field, California. *Journal of Volcanology and Geothermal Research*, *12*(3–4), 221–258. [https://doi.org/10.1016/0377-0273\(82\)90028-2](https://doi.org/10.1016/0377-0273(82)90028-2)
- Yukutake, Y., Ito, H., Honda, R., Harada, M., Tanada, T., & Yoshida, A. (2011). Fluid-induced swarm earthquake sequence revealed by precisely determined hypocenters and focal mechanisms in the 2009 activity at Hakone volcano, Japan. *Journal of Geophysical Research*, *116*(B4), B04308. <https://doi.org/10.1029/2010JB008036>
- Yukutake, Y., Yoshida, K., & Honda, R. (2022). Interaction between aseismic slip and fluid invasion in earthquake swarms revealed by dense geodetic and seismic observations. *Journal of Geophysical Research: Solid Earth*. <https://doi.org/10.1029/2021JB022933>
- Zaliapin, I., & Ben-Zion, Y. (2013). Earthquake clusters in Southern California I: Identification and stability. *Journal of Geophysical Research: Solid Earth*, *118*(6), 2847–2864. <https://doi.org/10.1002/jgrb.50179>
- Zaliapin, I., & Ben-Zion, Y. (2020). Earthquake declustering using the nearest-neighbor approach in space-time-magnitude domain. *Journal of Geophysical Research: Solid Earth*, *125*(4). <https://doi.org/10.1029/2018JB017120>
- Zaliapin, I., Gabrielov, A., Keilis-Borok, V., & Wong, H. (2008). Clustering analysis of seismicity and aftershock identification. *Physical Review Letters*, *101*(1), 018501. <https://doi.org/10.1103/PhysRevLett.101.018501>
- Zhai, G., Shirzaei, M., Manga, M., & Chen, X. (2019). Pore-pressure diffusion, enhanced by poroelastic stresses, controls induced seismicity in Oklahoma. *Proceedings of the National Academy of Sciences*, *116*(33), 16228–16233. <https://doi.org/10.1073/pnas.1819225116>
- Zhuang, J., & Touati, S. (2015). *Stochastic simulation of earthquake catalogs*. Community Online Resource for Statistical Seismicity Analysis. <https://doi.org/10.5078/CORSSA-43806322>
- Ziv, A., & Rubin, A. M. (2003). Implications of rate-and-state friction for properties of aftershock sequence: Quasi-static inherently discrete simulations. *Journal of Geophysical Research: Solid Earth*, *108*(B1). <https://doi.org/10.1029/2001JB001219>